Article

Molecular Cell

The Ubiquitin E3/E4 Ligase UBE4A Adjusts Protein Ubiquitylation and Accumulation at Sites of DNA Damage, Facilitating Double-Strand Break Repair

Graphical Abstract

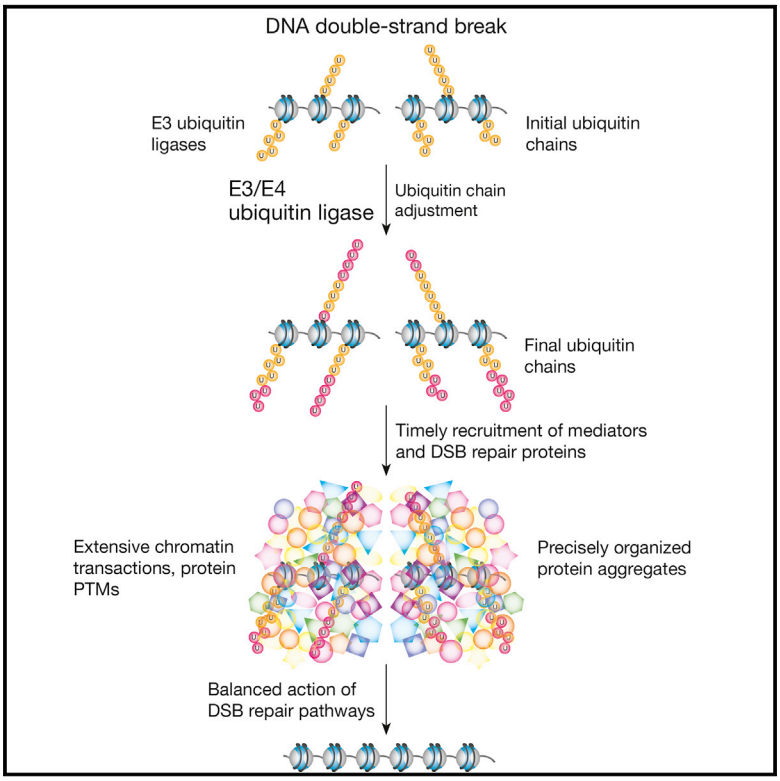

Highlights

- The E3/E4 ubiquitin ligase UBE4A is a new player in the DNA damage response
- UBE4A is required for optimal repair of DNA double-strand breaks
- After initial action of E3 ubiquitin ligases, UBE4A modulates ubiquitylation extent
- UBE4A's activity is required for appropriate balance of repair pathways

Authors

Keren Baranes-Bachar, Adva Levy-Barda, Judith Oehler, ..., Kristijan Ramadan, Yael Ziv, Yosef Shiloh

Correspondence

yossih@post.tau.ac.il

In Brief

The DNA damage response is activated by DNA double-strand breaks (DSBs) and involves protein ubiquitylation. Baranes-Bachar et al. show that, following initial ubiquitylation at DSB sites by E3 ubiquitin ligases, ubiquitin chains require further modulation by an E3/E4 ligase, UBE4A, to achieve optimal DSB repair.

Baranes-Bachar et al., 2018, Molecular Cell 69, 866–878
March 1, 2018
https://doi.org/10.1016/j.molcel.2018.02.002

CellPress

CellPress

Molecular Cell
Article

The Ubiquitin E3/E4 Ligase UBE4A Adjusts Protein Ubiquitylation and Accumulation at Sites of DNA Damage, Facilitating Double-Strand Break Repair

Keren Baranes-Bachar,[1] Adva Levy-Barda,[1] Judith Oehler,[2] Dylan A. Reid,[3] Isabel Soria-Bretones,[4] Ty C. Voss,[5] Dudley Chung,[6] Yoon Park,[7] Chao Liu,[8] Jong-Bok Yoon,[7] Wei Li,[8] Graham Dellaire,[6] Tom Misteli,[5] Pablo Huertas,[4] Eli Rothenberg,[3] Kristijan Ramadan,[2] Yael Ziv,[1] and Yosef Shiloh[1,9,*]

[1]The David and Inez Myers Laboratory for Cancer Research, Department of Human Molecular Genetics and Biochemistry, Sackler School of Medicine, Tel Aviv University, Tel Aviv, Israel

[2]Cancer Research UK and Medical Research Council Oxford Institute for Radiation Oncology, Department of Oncology, University of Oxford, Oxford, UK

[3]Perlmutter NYU Cancer Center and Department of Biochemistry and Molecular Pharmacology, New York University School of Medicine, New York, NY, USA

[4]Centro Andaluz de Biología Molecular y Medicina Regenerativa (CABIMER) and Department of Genetics, University of Sevilla, Sevilla, Spain

[5]National Cancer Institute, NIH, Bethesda, MD, USA

[6]Departments of Pathology and Biochemistry and Molecular Biology, Dalhousie University, Halifax, NS, Canada

[7]Department of Biochemistry and Protein Network Research Center, Yonsei University, 134 Shinchon-Dong, Seodaemoon-Gu, Seoul, Korea

[8]State Key Laboratory of Stem Cell and Reproductive Biology, Institute of Zoology, Chinese Academy of Sciences, Beijing, China

[9]Lead Contact

*Correspondence: yossih@post.tau.ac.il

https://doi.org/10.1016/j.molcel.2018.02.002

SUMMARY

Double-strand breaks (DSBs) are critical DNA lesions that robustly activate the elaborate DNA damage response (DDR) network. We identified a critical player in DDR fine-tuning: the E3/E4 ubiquitin ligase UBE4A. UBE4A's recruitment to sites of DNA damage is dependent on primary E3 ligases in the DDR and promotes enhancement and sustainment of K48- and K63-linked ubiquitin chains at these sites. This step is required for timely recruitment of the RAP80 and BRCA1 proteins and proper organization of RAP80- and BRCA1-associated protein complexes at DSB sites. This pathway is essential for optimal end resection at DSBs, and its abrogation leads to upregulation of the highly mutagenic alternative end-joining repair at the expense of error-free homologous recombination repair. Our data uncover a critical regulatory level in the DSB response and underscore the importance of fine-tuning the complex DDR network for accurate and balanced execution of DSB repair.

INTRODUCTION

Maintenance of genome stability is critical for cellular homeostasis, streamlined development, and prevention of undue cell death, cancer, and premature aging. A major axis in maintaining genome stability is the DNA damage response (DDR), a broad network that activates DNA repair mechanisms and sets in motion an elaborate series of events that swiftly modulate numerous physiological processes (Goldstein and Kastan, 2015; Sirbu and Cortez, 2013). The highly cytotoxic double-strand break (DSB) provokes a robust and highly coordinated response of the DDR network (Goldstein and Kastan, 2015; Goodarzi and Jeggo, 2013; Shiloh and Ziv, 2013; Sirbu and Cortez, 2013).

DSBs are repaired mainly by end resection-independent, canonical non-homologous end joining (C-NHEJ) or resection-dependent homologous recombination repair (HRR) (Chang et al., 2017; Kowalczykowski, 2015). The predominant repair pathway is C-NHEJ, in which broken ends are processed and rejoined; it operates throughout the cell cycle. HRR is based primarily on homologous recombination between the damaged DNA molecule and its intact sister and, therefore, is active in the late S and G2 phases of the cell cycle. Minor resection-dependent pathways are single-strand annealing (SSA), and alternative NHEJ (alt-NHEJ) (also referred to as microhomology-mediated end joining) (Chang et al., 2017). These pathways are based on annealing of sequences of different lengths in the 3′ overhangs generated by 5′ end resection (Symington, 2016). Although HRR is error-free, the other pathways are variably error-prone. A delicate balance between these repair pathways is essential for orderly completion of DSB sealing, and its abrogation may retard DSB repair and enhance genome aberrations (Shibata and Jeggo, 2014). Many players in the DSB response relocate to DSB sites, where they form large protein hubs (Lukas et al., 2011). These proteins typically undergo post-translational modifications (PTMs), primarily poly(ADP-ribosylation), phosphorylation, and modification by the ubiquitin (Ub) family proteins, which set them up to operate in the DDR (Harding and Greenberg, 2016; Lee et al., 2017; Martin-Hernandez et al., 2017; Polo and Jackson, 2011; Shiloh and Ziv, 2013; Wilson and Durocher, 2017). This massive protein recruitment is a highly

structured process in which the damage-induced PTMs often establish interactions among the proteins to help mobilize and correctly locate the next-in-line recruits. Interference with this process usually leads to abrogation of DSB repair. The chief transducer of the signal emanating from the DSB sites is the protein kinase ataxia-telangiectasia, mutated (ATM), which phosphorylates a plethora of substrates at these sites and elsewhere (Paull, 2015; Shiloh and Ziv, 2013).

Protein ubiquitylation at DSB sites is carried out by several E3 ubiquitin ligases and is critical for mobilizing chromatin dynamics at these sites, appropriate recruitment of DDR factors, and, eventually, DSB repair (Harding and Greenberg, 2016; Lee et al., 2017). Indeed, extensive K48- and K63-linked ubiquitylations were observed at DSB sites (Lee et al., 2017; Meerang et al., 2011), but the number of documented ubiquitylation targets is limited, and current consensual substrates are histones H2A, H2B, and H1 (Harding and Greenberg, 2016; Lee et al., 2017). Identification of the ubiquitin ligases that take part in the DDR is key to understanding ubiquitin-driven pathways in this network. Major factors in H2A ubiquitylation are the E3 ligases RNF8 and RNF168, whose activity is required for proper recruitment of the 53BP1 protein—a platform for additional DDR proteins and a regulator of DSB repair pathway choice—and RAP80, which anchors the protein complex BRCA1-A, whose subsequent dynamics play a role in the critical balance between DSB repair pathways (Lombardi et al., 2017).

Among the various families of E3 ubiquitin ligases, a small subgroup of the RING-type ligases contains a modified RING domain called U-box, which, like the RING domain, is essential for the enzyme's catalytic activity (Aravind and Koonin, 2000). One of the best-characterized U-box ligases is the yeast protein ubiquitin fusion degradation 2 (Ufd2), which has been associated with endoplasmic reticulum-associated protein degradation (ERAD) (Johnson et al., 1995). Ufd2 also possesses an E4 ligase activity. E3 ligases with E4 activity (E3/E4 ligases) can bind to a single conjugated ubiquitin or an oligoubiquitin chain generated by other E3 ligases and further extend and regulate the lengths of the chains (Hatakeyama et al., 2001; Hoppe, 2005). Ufd2 is conserved throughout evolution, with two orthologs in mammals that are likely paralogs, designated in humans UBE4A and UBE4B. UBE4B's E4 ligase activity has been demonstrated, and among its substrates are p53 and ataxin-3 (Du et al., 2016; Hatakeyama and Nakayama, 2003; Matsumoto et al., 2004; Park et al., 2008, 2009; Periz et al., 2015; Starita et al., 2013; Wu and Leng, 2011; Wu et al., 2011). UBE4A's activity and physiological significance have not been extensively documented. Recently it has been implicated in targeting interleukin-like EMT inducer for degradation (Sun et al., 2017).

Here we show that UBE4A is a critical DDR factor. It has an E4 ubiquitin ligase activity *in vitro*, and in cells its presence is required for tweaking the extent of both K48- and K63-linked ubiquitin chains at sites of DNA damage. Acting downstream of the primary E3 ligases in the DDR and 53BP1, UBE4A's action in fine adjustment of ubiquitin chain length is required for proper internal organization of DSB-associated protein foci and, ultimately, for maintaining the exquisite balanced between DSB repair pathways and timely DSB repair.

RESULTS

UBE4A Is Essential for Appropriate Cellular Response to DSBs

Our attention was drawn to UBE4A and UBE4B when UBE4B was identified as a hit in a functional screen we carried out in search of novel determinants of ubiquitylation in the DDR (Figure S1; Tables S1, S2, and S3). In view of their sequence similarity, we explored the possibility that both proteins are involved in the DDR. Initial experiments indicated that this was the case, but UBE4A and UBE4B seemed to function separately in different DDR branches. Here we focus on UBE4A, the less studied paralog (Figure 1A). The first indication that UBE4A functions in the DSB response came from the observation that its depletion led to cellular hypersensitivity to the radiomimetic drug neocarzinostatin (NCS) in a clonogenic survival assay (Figure 1B). Such sensitivity is suggestive of defective DSB repair. To directly examine the effect of UBE4A depletion on DSB sealing, we used the sensitive neutral comet assay (Glei et al., 2016) to measure the amount of DSBs remaining in genomic DNA after treatment with ionizing radiation (IR). Significant differences in comet tail moment (an actual measure of DSBs in the neutral comet assay) were observed between UBE4A-proficient and -depleted cells 24 hr after IR treatment (Figure 1C), indicating a marked, continuous retardation in DSB closure upon reduction of the UBE4A level. Similarly, UBE4A depletion led to retarded disappearance of nuclear foci of the DDR protein 53BP1 24 hr after treatment with NCS (Figure 1D). Importantly, ectopic expression of wild-type UBE4A in cells depleted of the endogenous protein complemented the defective repair phenotype, whereas a potentially inactive mutant protein lacking the U-box failed to do so (Figure 1D), suggesting that the catalytic activity of UBE4A is essential for its function in DSB repair.

UBE4A Is Recruited to Sites of DNA Damage Dependent on Major E3 Ligases in the DDR and 53BP1

A common attribute of many DSB response players is their temporary relocation to damage sites. In view of the above results, we asked whether UBE4A undergoes such relocation. The dynamics of this recruitment are usually monitored after induction of localized DNA damage in a narrow nuclear sector using a focused laser microbeam. We observed relocalization to such "laser stripes" of a portion of ectopic, GFP-tagged UBE4A within minutes of damage induction (Figure 2A). Mutant protein lacking the U-box was recruited at similar kinetics (Figure 2A), indicating that UBE4A's catalytic activity was not required for this process. We further demonstrated UBE4A's recruitment to damage sites by following the relocation of endogenous UBE4A to laser stripes using a specific antibody (Figure 2B). The data thus establish that UBE4A is part of the large cohort of proteins that function at DSB sites and are required for efficient DSB repair.

The formation of the protein hubs spanning DSBs is a structured, hierarchical process, and the precise order of protein relocalization to the break sites reflects the dependence of each protein's recruitment on previously recruited ones. To place UBE4A in this hierarchy, we examined the dependence of its recruitment on selected proteins in the cascade. In this list, depletion of 53BP1 and the E3 ubiquitin ligases RNF8 and

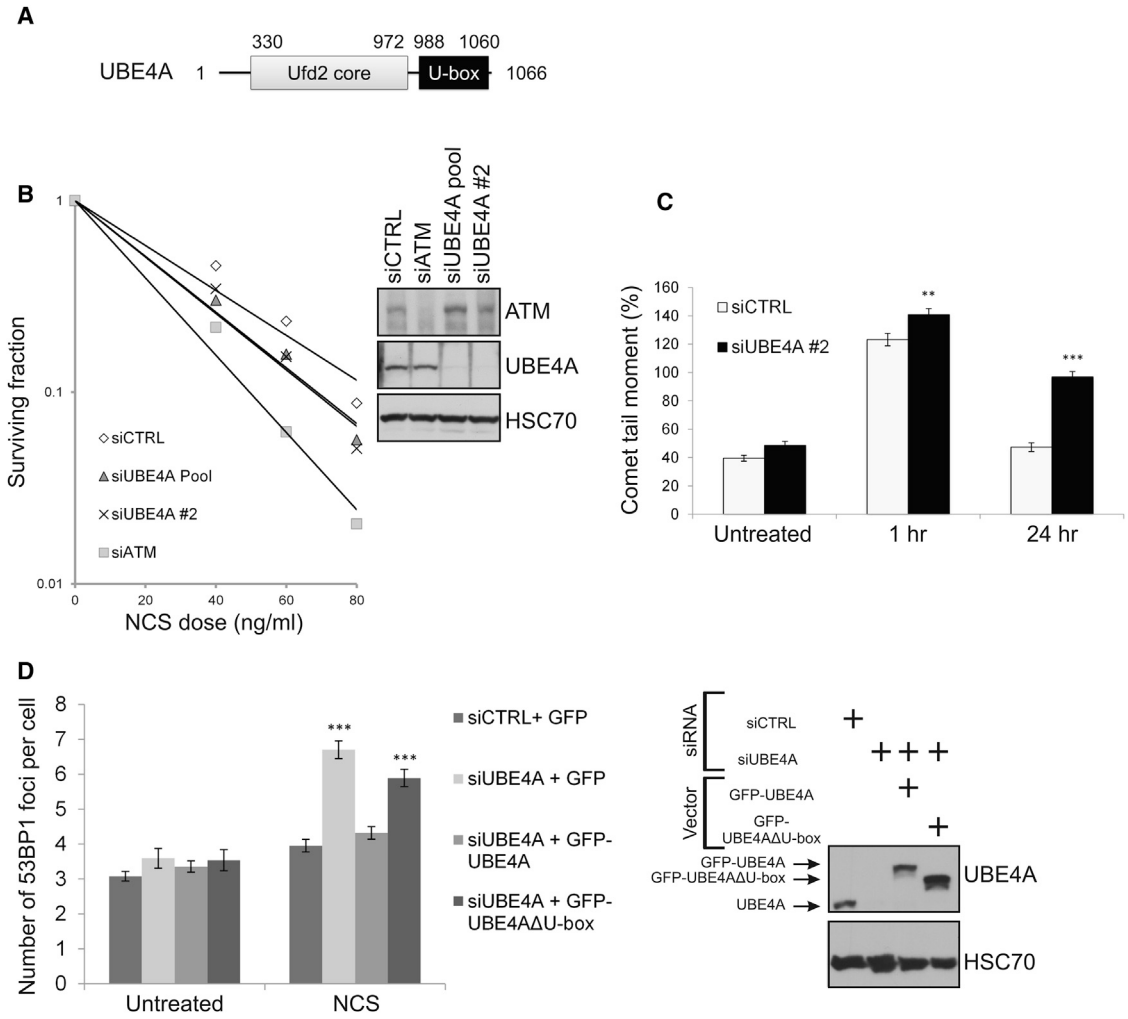

Figure 1. UBE4A Depletion Affects DSB Repair

(A) Domain diagram of UBE4A.

(B) UBE4A depletion leads to cellular hypersensitivity to the radiomimetic chemical NCS. Clonogenic survival curves of CAL51 cells transfected with control siRNA (siCTRL) or two siRNAs directed against UBE4A and subsequently treated with various NCS doses. siCTRL cells and cells transfected with siATM served as controls. The immunoblot shows the degree of protein depletion for UBE4A and ATM.

(C) Direct observation of DSBs in UBE4A-proficient and -depleted A549 cells using a neutral comet assay 1 and 24 hr after irradiation with 10 Gy of IR.

(D) Numbers of 53BP1 nuclear foci in cells 24 hr after treatment with 20 ng/mL of NCS. Cells were transfected with the indicated siRNAs and with vectors expressing GFP or siRNA-resistant cDNAs encoding GFP-tagged wild-type UBE4A or mutant UBE4A lacking the U-box (GFP-UBE4AΔU-box). The immunoblot shows the extent of endogenous UBE4A depletion and expression of ectopic proteins.

RNF168 markedly affected UBE4A recruitment, and depletion of the E3 ligase RNF4 moderately reduced it (Figures 2C, S2A, and S2B). These E3 ligases drive a major ubiquitylation cascade at DSB sites that is essential for DSB repair. Thus, our results suggest that timely appearance of UBE4A at damage sites depends on prior protein ubiquitylation at these sites and on prior presence at these sites of 53BP1—a central regulator of the choice between DSB repair pathways (Daley and Sung, 2014; Gupta et al., 2014).

The yeast ortholog of UBE4A and UBE4B, Ufd2, functions in close collaboration and physical association with the ATPase Cdc48, and with the Rad23 protein (Baek et al., 2013). The human ortholog of Cdc48, p97/VCP, was recently reported to play a role in the DSB response (Torrecilla et al., 2017). The mammalian paralogs of Rad23, RAD23A and RAD23B, are involved in the response to bulky DNA lesions via the nucleotide excision repair pathway (Yokoi and Hanaoka, 2017). We therefore examined the possible dependence of UBE4A's recruitment to damage sites on these proteins. We found that RAD23A, RAD23B, and VCP were not required for UBE4A recruitment to damage sites, nor was UBE4A's paralog, UBE4B, necessary for this process (Figures 2C, S2A, and S2C). Furthermore, depletion of UBE4A did not affect the recruitment of the DDR proteins RNF8, RNF168, 53BP1, and MDC1 or γH2AX formation (Figure S2D). These experiments place UBE4A at a relatively late stage in the hierarchy of protein assembly at DSB sites, with

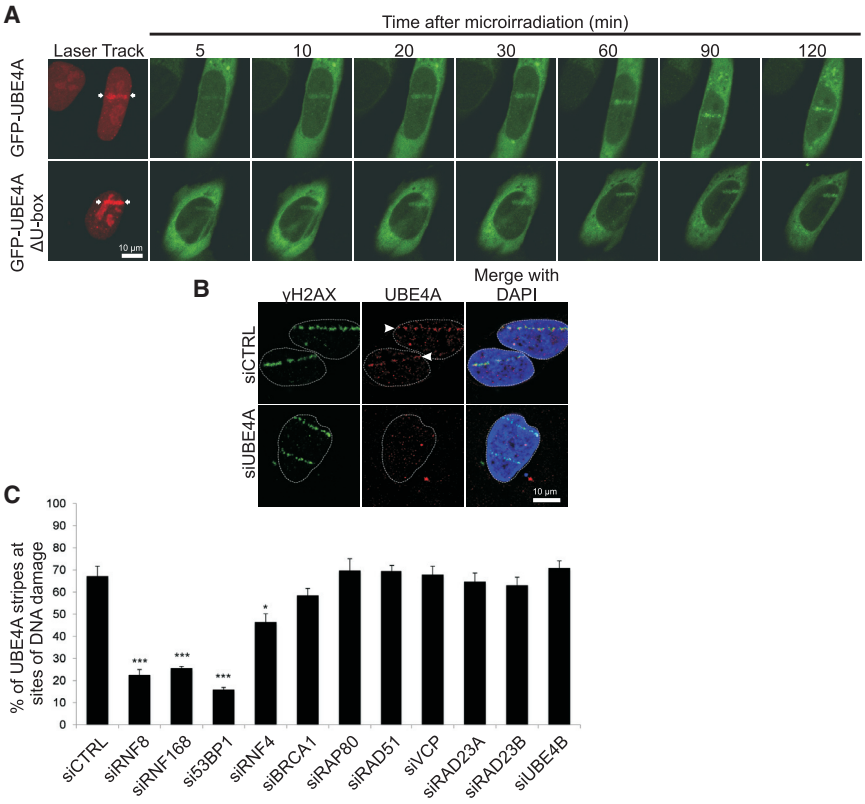

Figure 2. UBE4A Relocalizes to Sites of DNA Damage Dependent on Other E3 Ligases and 53BP1

(A) Dynamics of UBE4A relocalization to damage sites in live cells. Cells were depleted of endogenous UBE4A using RNAi and co-transfected with vectors expressing siRNA-resistant cDNAs of GFP-UBE4A or GFP-UBE4AΔU-box together with DsRed2-tagged polynucleotide kinase-phosphatase (PNKP). The rapid recruitment of PNKP to damage sites (red) (Segal-Raz et al., 2011) marks their location. Localized DNA damage was induced using a focused laser microbeam, and the cells were monitored by time-lapse imaging. Note the rapid recruitment to laser-induced damage sites of both wild-type and mutant UBE4A (green).

(B) Recruitment of endogenous UBE4A to sites of laser-induced damage. Cells were transfected with siRNA against UBE4A or irrelevant siRNA, treated with laser microirradiation, and immunostained 40 min later with antibodies against UBE4A and γH2AX.

(C) Using the same experimental setup as in (B), the cells were transfected with the indicated siRNAs, treated with laser microirradiation, and monitored for recruitment of endogenous UBE4A to damage sites 20 min later. The fraction of γH2AX stripes co-stained for UBE4A was recorded and is presented as mean ± SD (3 independent experiments, n = 200). *$p < 0.05$, ***$p < 0.0005$ (Student's t test).

See also Figure S2.

dependence on prior protein ubiquitylation within these protein assemblies and downstream of 53BP1. Interestingly, we found that UBE4A co-immunoprecipitates with 53BP1 and that this co-immunoprecipitation is enhanced by DNA damage (Figure S2E). This observation and the 53BP1 dependence of UBE4A recruitment suggest that UBE4A's entry into the DSB response cascade is mediated at least in part by direct or indirect interaction with 53BP1.

UBE4A Activity and UBE4A-Dependent Modulation of K48- and K63-Linked Ubiquitin Chains at Damage Sites

We assumed that UBE4A functions at DSB sites in its capacity as an E4 ubiquitin ligase, an activity that was previously demonstrated in its paralog, UBE4B. To demonstrate UBE4A's E4 activity, we carried out an experiment similar to a previous one that showed UBE4B's E4 activity *in vitro* (Park et al., 2009). The UFD pathway can be probed in cells and *in vitro* using an artificial substrate, monoubiquitylated GFP (Dantuma et al., 2000). Using such a substrate, in which the ubiquitin moiety is mutated and thus uncleavable (Ub^{G76V}), Park et al. (2009) previously found that the HECT domain E3 ligase TRIP12 functions in the UFD pathway in mammalian cells, but for optimal ubiquitylation of the substrate, TRIP12's activity should be followed by the E4 activity of UBE4B (). This requirement for both the E3 and E4 ligases for optimal substrate ubiquitylation was demonstrated *in vitro* (Park et al., 2009). In an analogous experiment, we used the same *in vitro* system, only with UBE4A as the E4 ligase (Figures 3 and S3A). We found that, similarly to its paralog, UBE4B (Park et al., 2009), UBE4A functions in this reaction as an E4 ligase. Further evidence for UBE4A's involvement in protein ubiquitylation in cells was obtained by examining the effect of its depletion on cellular protein ubiquitylation using a method developed recently to pull down ubiquitylated proteins from cellular extracts (Sims et al., 2012). According to this method, ubiquitin-interacting motif domains (UIMs) are expressed in cells and are subsequently immunoprecipitated using an attached tag that pulls down interacting proteins. We used a construct containing 3 tandem UIMs derived from the DDR protein RAP80 that selectively bind K63-linked ubiquitin chains (Sims et al., 2012; Thorslund et al., 2015). Indeed, UBE4A depletion decreased the amount of K63-linked ubiquitylation in unirradiated cells and cells irradiated with X-rays (Figure S3B), suggesting a role for UBE4A in shaping protein ubiquitylation in cells in several ubiquitin-driven processes, similar to its paralog UBE4B.

The E4 ligase function is plausibly broad and used in various physiological contexts. Accordingly, E3/E4 ligases have broad specificity with regard to the types of ubiquitin chains they extend, which may depend on the combinations of E2 and E3 ligases in specific reactions (Ackermann et al., 2016; Hatakeyama and Nakayama, 2003; Hoppe, 2005; Liu et al., 2017; Matsumoto et al., 2004; Park et al., 2008, 2009; Saeki et al., 2004; Wu and Leng, 2011; Wu et al., 2011). UBE4B was shown to extend K27-, K33-, and K48-linked chains (Hatakeyama and Nakayama, 2003; Hatakeyama et al., 2001; Park et al., 2008, 2009; Wu and Leng, 2011; Wu et al., 2011). Yeast Ufd2 catalyzes the extension of K29- and K48-linked chains (Ackermann et al., 2016; Saeki

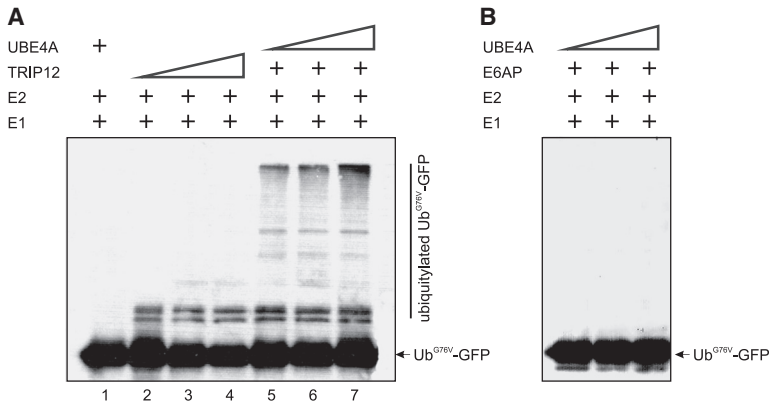

Figure 3. E4 Ligase Activity of UBE4A *In Vitro*

(A) His6-Ub^{G76V}-GFP (300 ng) was incubated for 1 hr at 37°C with FLAG-TRIP12 (200 and 400 ng in lanes 2 and 3, respectively, and 800 ng in lanes 4–6) and FLAG-UBE4A (250 and 500 ng in lanes 5 and 6, respectively, and 1000 ng in lanes 1 and 7) in a reaction mixture containing 2 mM ATP, 800 ng of His6-Ub, 100 ng of His6-Uba1, and 250 ng of His6-UbcH5a. The reaction was terminated by addition of 2× Laemmli sample buffer and subjected to SDS-PAGE. The blot was subsequently probed with an anti-GFP antibody.

(B) Similar reactions as in (A), with another E3 ligase, E6AP, replacing TRIP12.

See also Figure S3.

et al., 2004) and creates branched chains by catalyzing K48-linked multi-monoubiquitylation on K29-linked ubiquitin chains (Liu et al., 2017). *C. elegans* Ufd-2 extends K29- and K48-linked chains (Ackermann et al., 2016) as well as K63-linked chains (W. Pokrzywa and T. Hoppe, personal communication). DSB sites are characterized by extensive K48- and K63-linked protein ubiquitylation (Meerang et al., 2011; Ramadan, 2012). We asked whether UBE4A was involved in extending these chain types at sites of DNA damage. Previous work showed that K48-linked ubiquitylation at damage sites mounts rapidly, peaks 15 min after damage induction, and decreases sharply within the next hour, whereas K63-linked ubiquitylation peaks 1 hr after damage induction and persists for several hours (Meerang et al., 2011; Ramadan, 2012). These experiments were based on quantitating the signal obtained at laser stripes after immunostaining with antibodies specific for these ubiquitin chain types. Cells depleted for the p97/VCP protein serve as controls in these experiments because loss of this protein leads to excessive accumulation of ubiquitylated proteins at damage sites (Meerang et al., 2011).

We quantified the average intensity of K48- and K63-linked ubiquitylation at DNA damage sites using antibodies specific for these chain types (Figure S4A). UBE4A depletion markedly decreased but did not eliminate the average K48 signal 15 min after damage induction, and the effect was diminished 2 hr later, when the K48 signal usually subsided (Figures 4A, 4B, and S4B). When we classified the ubiquitin signals as "strong," "average." and "undetectable" (Figure S4C), cells depleted of UBE4A had a significantly lower fraction of strong K48 stripes and a higher fraction of undetectable stripes 15 min after damage induction compared with control (irrelevant) small interfering RNA (siCTRL)-treated cells (Figure 4C). This implies that UBE4A is important for timely formation of K48-linked ubiquitin chains in proper amounts at the sites of DNA damage. Quantifying the intensity of K63-linked chains at the sites of DNA damage showed that depletion of UBE4A led to a lower average intensity of these chains relative to the control, both 15 min and 2 hr after induction of DNA damage (Figures 4D, 4E, and S4D). Accordingly, UBE4A depletion led to a markedly higher fraction of cells with undetectable K63-linked chain signals at damage sites compared with siCTRL and a lower fraction of average- and strong-intensity chain signals (Figure 4F). Taken together, these data establish that UBE4A is critical for the required timing and amount of two major types of ubiquitylation that occur ubiquitously at sites of DNA damage: K48-linked ubiquitylation, which marks target proteins for proteasome-mediated degradation, and K63-linked chains, which alter the protein function or mode of action (Spasser and Brik, 2012; Williamson et al., 2013).

UBE4A Is Required for Complete Assembly of Specific DDR Factors at DSB Sites and Proper Internal Organization of DSB-Associated Protein Foci

An important outcome of K63-linked ubiquitylation at DSB sites is the recruitment of the DDR factor RAP80, which has specific affinity for these ubiquitin chains because of its tandem UIMs (Lombardi et al., 2017). Indeed, UBE4A depletion led to reduced accrual of RAP80 at DNA breaks (Figure 5A) in a manner that was dependent on UBE4A activity (Figure 5B). A further consequence of UBE4A depletion was reduced recruitment of BRCA1, which is dependent on RAP80 (Figure 5C). RAP80 recruitment was not completely abolished, however, because UBE4A depletion does not completely eliminate protein ubiquitylation at damage sites (Figure 4). Further downstream is the major HRR protein RAD51, and here, too, damaged UBE4A-depleted cells exhibited a significantly lower number of nuclear RAD51 foci at the S and G2 cell cycle phases (in which HRR functions) (Figure 5D).

When these proteins are recruited to DSB sites, their precise assembly there in space and time and the dynamics of the internal focus organization are critical for proper DSB repair (Lukas et al., 2011). To study this organization, we used single-molecule localization-based super-resolution (SR) imaging, a powerful form of fluorescent microscopy that offers a 10-fold improvement over conventional diffraction-limited microscopy such as confocal microscopy (Huang et al., 2009). The modality was recently used to examine the organization of DSB repair proteins at damage sites (Conlin et al., 2017; Reid et al., 2015; see Figures 6A and 6B for examples). To generate SR images, we used direct stochastic optical reconstruction microscopy (dSTORM) to localize single fluorescent dye molecules below the diffraction limit (van de Linde et al., 2011). In dSTORM, fluorescent dyes are predominately in a dark state (not fluorescing) because of the presence of the chemical mercaptoethylamine (MEA). However, at any given time, a small, sparse subset of fluorophores emits fluorescence, permitting their localization. This population

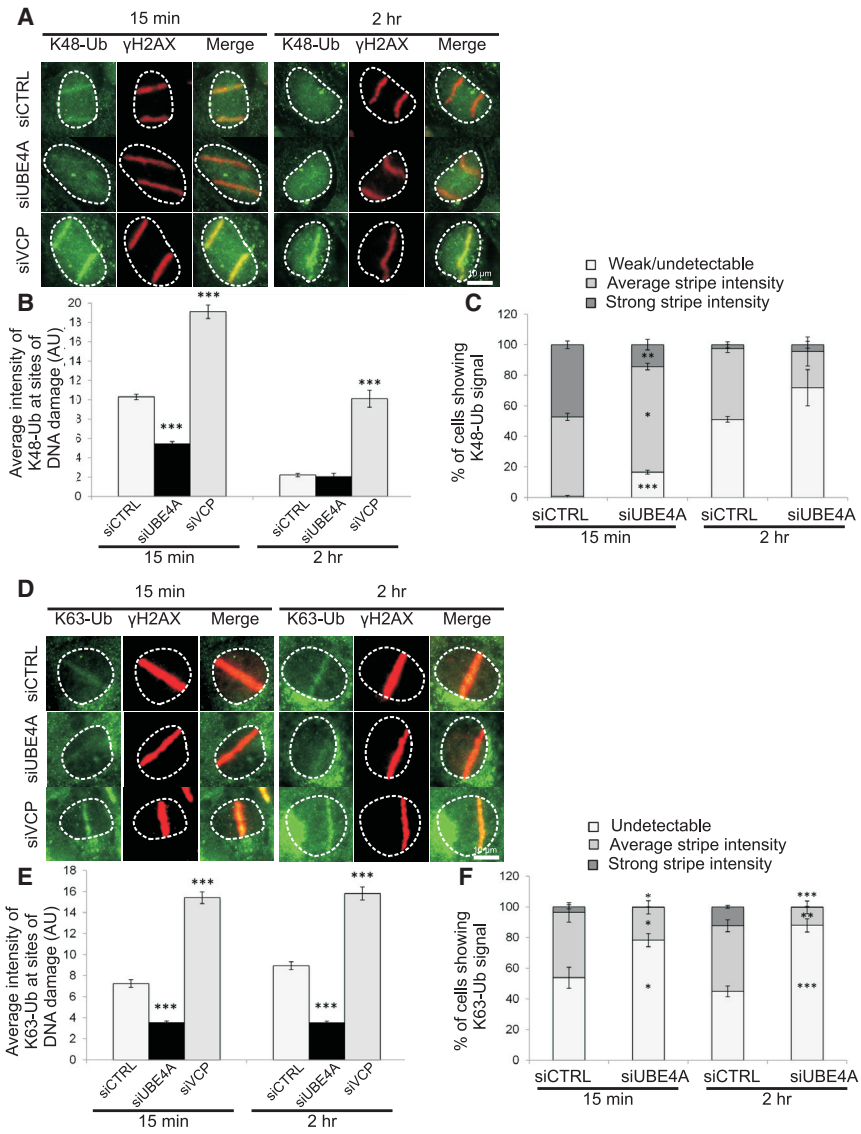

Figure 4. UBE4A Is Required for Timely and Quantitatively Proper Assembly of Ubiquitin Chains at Sites of DNA Damage

(A) Cells were transfected with the indicated siRNAs, and localized DNA damage was induced using a focused laser microbeam. The cells were fixed 15 min or 2 hr later and stained with antibodies against γH2AX and K48-Ub.

(B) The accumulation of K48-Ub was quantified according to the fluorescence intensity obtained using the corresponding antibody on top of γH2AX stripes. The immunoblot shows the extent of UBE4A depletion in this experiment.

(C) K48-Ub lines were classified as strong, average, or weak/undetectable.

(D–F) Similar analysis as in (A)–(C) for K63-linked ubiquitin chains.

The quantified data in (B) and (C) are represented as mean ± SEM (3 independent experiments, n > 70) and in (E) and (F) as mean ± SEM (4 independent experiments, n > 80). *p < 0.05, **p < 0.005, ***p < 0.0005 (Student's t test, relative to the siCTRL). See also Figure S4. AU, arbitrary units.

changes stochastically, and by acquiring a series of images from a viewing field, a super-resolved image can be generated with coordinates of each localized molecule. Researchers recently used this approach to study the structure of DNA damage-associated protein foci (Britton et al., 2013; Doksani et al., 2013; Reid et al., 2015; Young et al., 2015) as well as other systems that challenge imaging because of a size that is close to the diffraction limit, such as neuronal synapses (Dani et al., 2010). Moreover, because single dyes are localized, this technique is substantially more sensitive than other SR techniques, so analysis is not necessarily confined to the brightest foci. Here the information obtained allows us to make quantitative determinations, such as the area occupied by various proteins (Wani et al., 2016), that might be missed with conventional imaging. In addition, we can measure the degree of overlap between proteins (Figures 6A and 6B), yielding information about the spatial organization and physical proximity among proteins within the focus. These parameters may point to the intactness of the processes in which these protein function. Because UBE4A depletion affected the recruitment of RAP80, BRCA1, and RAD51 (Figure 5), we focused on these proteins as well as two other HRR factors, BRCA2 and PALB2.

RAP80 mediates the recruitment of the BRCA1-A complex, which includes BRCA1, RAP80, ABRAXAS, and MERIT40 and antagonizes HRR (Coleman and Greenberg, 2011). This barrier to HRR is subsequently removed during spreading and repositioning of the BRCA1-A complex and formation of the BRCC complex, which includes BRCA1, BRCA2, PALB2, and RAD51 and drives HRR (reviewed by Park et al., 2014). Notably, the spatial distribution of RAP80 foci determined here using dSTORM (~0.3–0.4 μm^2; Figure S5) was similar to that reported previously using correlative light and electron microscopic imaging of γH2AX foci (Dellaire et al., 2009). We also found that, compared with controls, the areas occupied by RAP80 and BRCA1 were larger in UBE4A-depleted cells at early time points (5–30 min after damage induction) and returned to normal values 6 hr later (Figures 6C–6E, S5A, and S5B). On the other hand, the areas occupied by BRCA2 and PALB2 after UBE4A depletion were smaller than in control cells (Figure 6C). Accordingly, UBE4A depletion led to increased overlaps of RAP80 and BRCA1 with γH2AX and decreased these overlaps for BRCA2, PALB2, and RAD51 (Figures 6D and 6E). The results suggested that UBE4A depletion caused an increased presence of the BRCA1-A complex and reduced presence of the BRCC complex at early time points after DSB induction, which could lead *a priori* to reduced HRR. Taken together, the

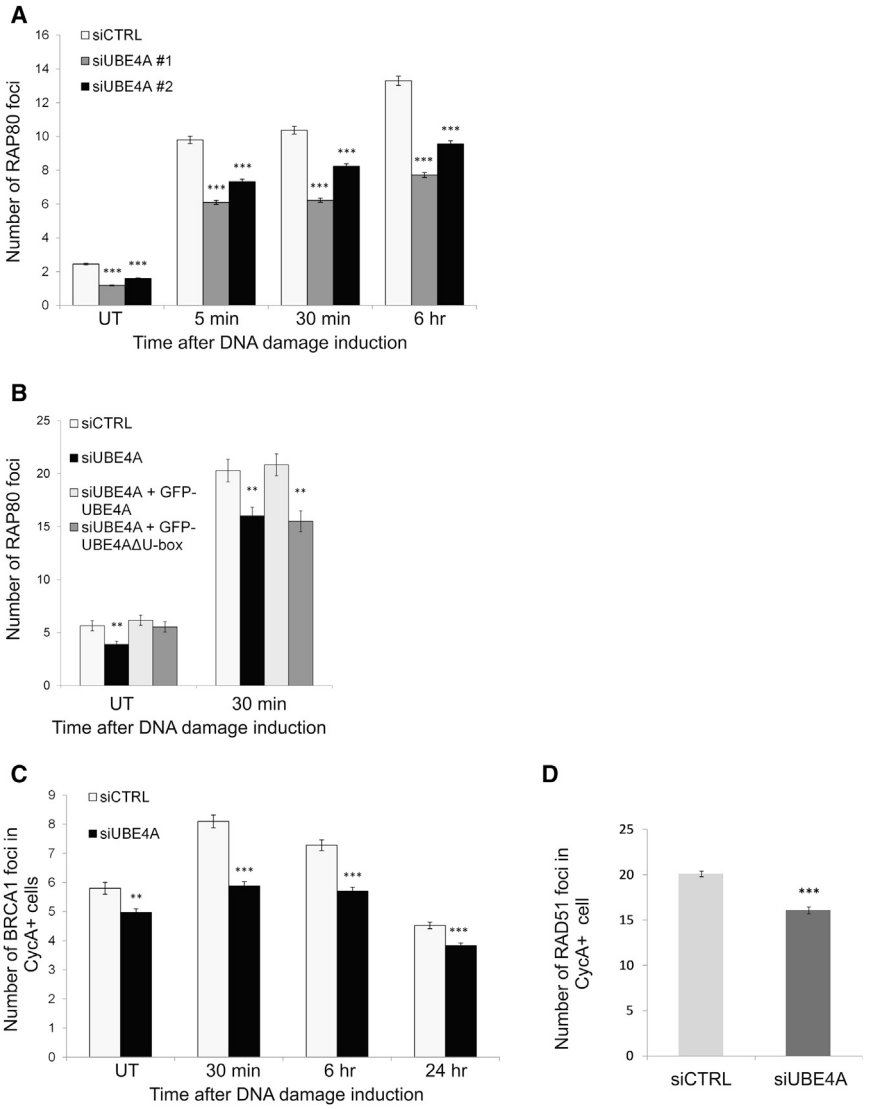

Figure 5. UBE4A Is Required for Assembly of Ubiquitin-Dependent Factors at Sites of DNA Damage in a U-box-Dependent Manner

(A) U2-OS cells were transfected with the indicated siRNA, treated with 20 ng/mL of NCS, and stained for nuclear foci of RAP80 at the indicated time points.

(B) U2-OS cells were transfected with irrelevant or siRNA against UBE4A, as well as constructs expressing siRNA-resistant wild-type GFP-UBE4A or GFP-UBE4A(ΔU-box). 48 hr later, the cells were treated with 20 ng/mL of NCS and stained for nuclear foci of RAP80.

(C) U2-OS cells were transfected with the indicated siRNA, treated with 20 ng/mL of NCS, and stained for nuclear foci of BRCA1 and cyclin-A2 at the indicated time points. BRCA1 foci were quantified in cyclin-A2-positive cells (i.e., cells at the S and G2 phases of the cell cycle).

(D) U2-OS cells were transfected with the indicated siRNA, treated with 1 Gy of IR, and, 1 hr later, stained for RAD51 and cyclin A2. Shown are percentages of cyclin A2-positive cells with more than 10 RAD51 foci/cell.

UT, untreated. The images in (A) and (C) were captured and analyzed using the Hermes WIScan apparatus. The images in (B) and (D) were captured using conventional fluorescence microscopy and analyzed using ImageJ software. Quantified data are presented as mean ± SEM. In (A) and (C): 2 independent experiments, n = 2,000. In (B): 2 independent experiments, n > 100. In (D): 3 independent experiments, n > 600. $^{**}p < 0.005$, $^{***}p < 0.0005$ (Student's t test, relative to the siCTRL).

results show that the recruitment of UBE4A downstream of 53BP1 and its E4 ligase activity are required for shaping up the protein ubiquitylation at DSB sites essential for optimal buildup of the protein array required for HRR (Figure 6F). We therefore proceeded to examine the interplay between DSB repair pathways upon UBE4A depletion.

A Shift from HRR to Alt-NHEJ upon UBE4A Depletion

HRR, the only error-free pathway, was evaluated in UBE4A-depleted cells using two different assays. The extensively documented DR-GFP reporter provides a fluorescent readout of HRR that takes place at a break induced by the restriction enzyme I-SceI (Pierce et al., 2001). This assay showed a moderate reduction in HRR upon UBE4A depletion (Figure 7A). A recently developed system for measuring the efficiency of homology-directed repair (HDR) is the CRISPR-LMNA HDR assay (Pinder et al., 2015; Figure S6). In this assay, a Cas9-generated DSB at the *LMNA* gene locus is repaired using a DNA homology donor encoding the GFP Clover, flanked by homology to the endogenous *LMNA* locus. Successful HDR between the homology donor and the *LMNA* locus results in expression of Clover-tagged LMNA and green fluorescence at the nuclear lamina. Depletion of UBE4A significantly reduced the efficiency of CRISPR-mediated HDR by 40% compared with an irrelevant small interfering RNA (siRNA), whereas a 70% reduction in HDR was conferred by depletion of a major HRR factor, RAD51 (Figure 7B). In parallel, we measured the effect of UBE4A depletion on C-NHEJ, alt-NHEJ, and SSA as well as the extent of end resection at DSBs. Importantly, although C-NHEJ and SSA were not affected, alt-NHEJ was increased in UBE4A-depleted cells (Figures 7C–7E). End resection, a key apical process in the decision among DSB repair pathways, was moderately reduced upon UBE4A depletion (Figure 7F). These results suggest that, following UBE4A depletion, end resection becomes suboptimal, and resection intermediates that cannot serve as HRR starting points are channeled to the highly error-prone alt-NHEJ (Figure 7G). Such a shift in the balance between repair pathways is also likely to leave unrepaired breaks (Figure 1C). Thus, the UBE4A-dependent pathway culminates in the exquisite regulation of the balance among DSB repair pathways.

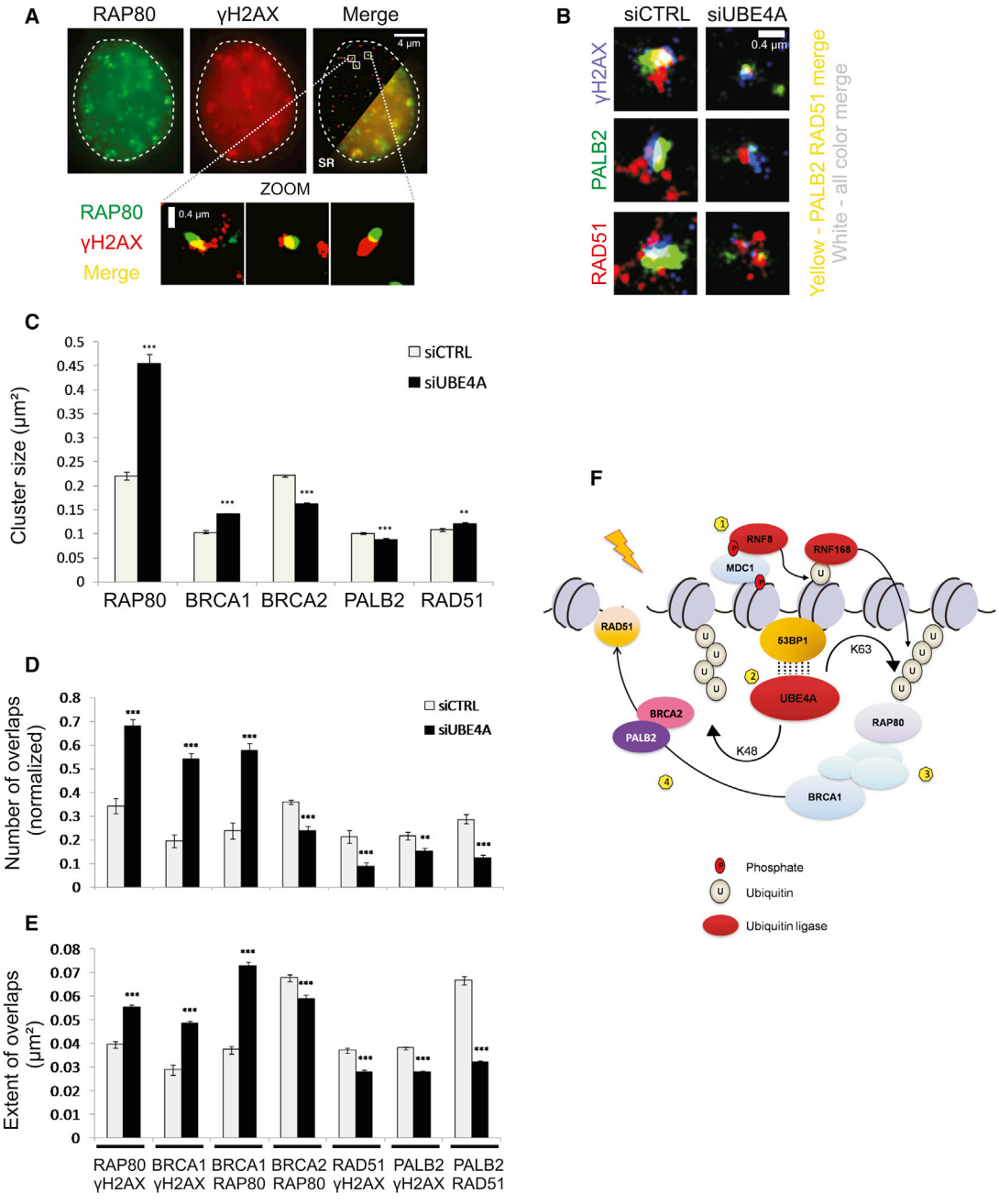

Figure 6. UBE4A Affects Focus Organization at Sites of DNA Damage

(A) Conventional diffraction limited total internal reflection fluorescence (TIRF) microscopy image of γH2AX and RAP80. Shown is a merged image with cutaway SR revealing the improved resolution. Bottom: selected zoomed regions showing γH2AX/RAP80 foci.

(B) Representative image of the overlaps of RAD51/PALB2/γH2AX focus particles in cells treated with control or UBE4A siRNAs and treated with NCS for 30 min.

(C) Quantification of the average area of focus particles (denoted as "cluster size") of various DDR proteins in cells treated with control or UBE4A siRNA and subsequently treated with NCS for 30 min.

(D) Quantification of the number of overlaps per nucleus (normalized to the total number of particles detected) between different pairs of DDR factors.

(E) Quantification of the extent of overlap between various DDR factors in cells treated with control or UBE4A siRNA and subsequently treated with NCS for 30 min.

(F) Molecular model for the role of UBE4A in ubiquitin signal enhancement. (1) The ubiquitin E3 ligases RNF8 and RNF168 are recruited to DSB sites and mediate protein ubiquitylation. (2) UBE4A is recruited in a 53BP1-dependent manner and regulates further adjustment of K48- and K63-linked ubiquitin chains. The dotted lines indicate a physical interaction that may be mediated by other proteins. (3) RAP80 is recruited to K63-Ub, thereby recruiting BRCA1 to form the BRCA1-A complex. (4) UBE4A promotes the dynamic reorganization of the BRCA1-A complex into the BRCC complex, which, in turn, promotes RAD51 recruitment and HRR.

See also Figure S5.

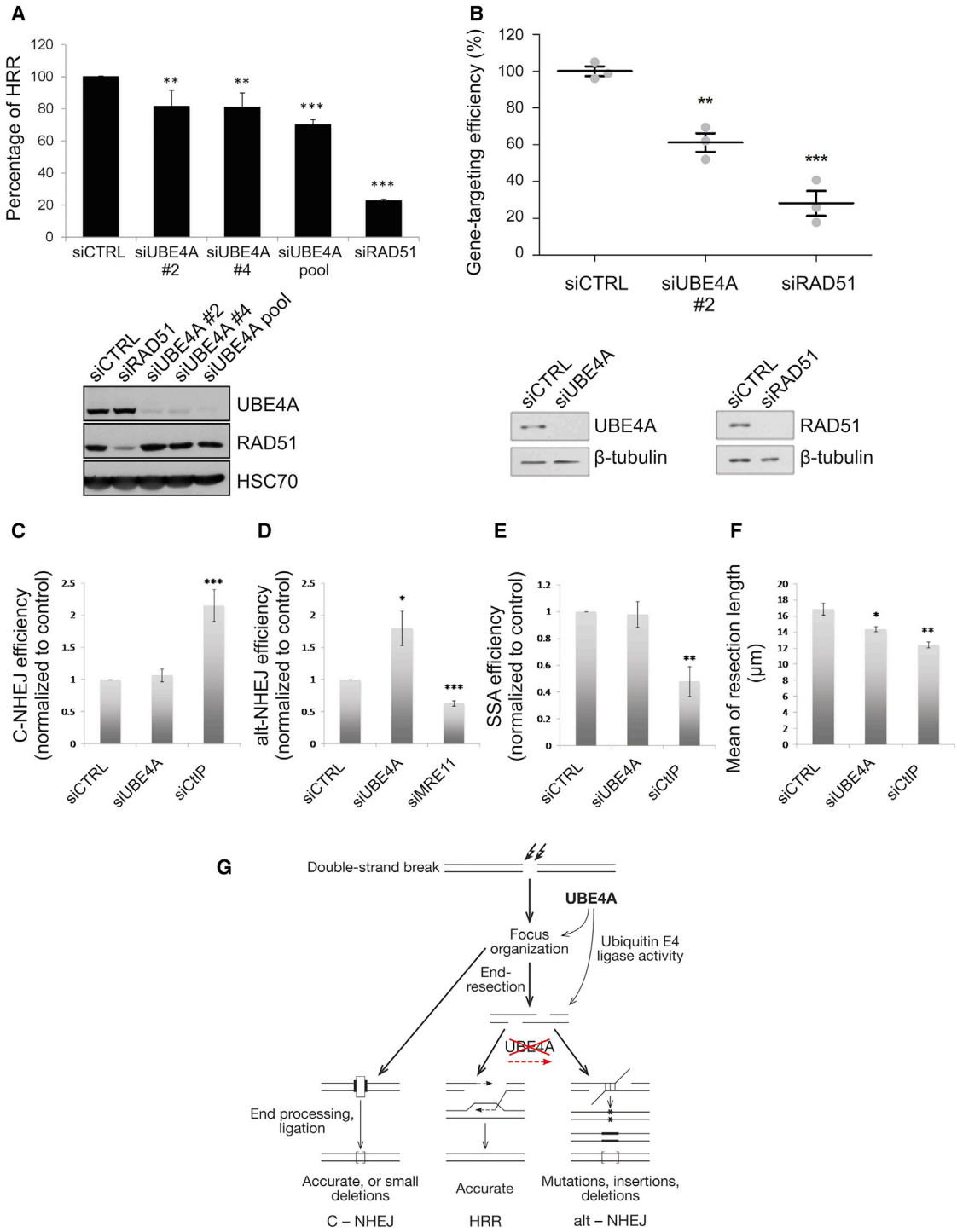

Figure 7. UBE4A Depletion Interferes with the Balance between DSB Repair Pathways

(A) HRR measurement based on the DR-GFP assay (Pierce et al., 2001). The siUBE4A pool includes four siRNA sequences: siRNA 1 to siRNA 4. Cells transfected with irrelevant siRNA or siRNA against RAD51, a major HRR protein, served as controls.

(B) CRISPR-mediated HDR. The CRISPR Clover-LMNA HDR assay (Pinder et al., 2015) was conducted in U2-OS cells in triplicate (n = 500–750 cells per replicate) and error bars = SEM. $^{**}p < 0.03$, $^{***}p < 0.001$ (Student's t test). The blots show the extent of protein depletion in this experiment. See also Figure S7.

(C–E) C-NHEJ (C), alt-NHEJ (D), and SSA (E) measured using the EJ5-GFP, EJ2-GFP, and SA-GFP reporters (Bennardo et al., 2008), respectively. In all cases, repair of an I-SceI meganuclease-induced DSB renders the cells GFP-positive when repair is achieved via the indicated pathway. The efficiency of repair was

(legend continued on next page)

DISCUSSION

The DSB response is an intricate, multi-level operation, and the activity within the massive protein hubs that form around DSBs attests to a highly complex cascade of events. Despite the complexity, this is a fine-tuned process that brings each DDR protein to the protein conglomerates spanning DSB sites at the precise time and location to perform the ultimate task: smooth and streamlined DSB repair. The importance of tight regulation of protein ubiquitylation in this process has been noted (Harding and Greenberg, 2016; Lee et al., 2017; Panier and Durocher, 2013). A primary level of this regulation is the universal balance between the relevant E3 ligases and opposing deubiquitylating proteases (DUBs) (Pellegrino and Altmeyer, 2016). Interestingly, the DUBs USP26 and USP27 were found to modulate RNF168-mediated protein ubiquitylation at DSB sites, preventing excessive spreading of RAP80-BRCA1, promoting association of BRCA1 with PALB2, and streamlining HRR (Typas et al., 2015), similar to the role we attribute to UBE4A. Another level of regulation is mediated by opposing actions of E3 ligases. The E3 ligase RNF169 was found to be recruited to DSB sites in an RNF8/RNF168-dependent manner and to attenuate ubiquitin-mediated signaling and accumulation of 53BP1 and RAP80 at damaged chromatin, stimulating HRR and restraining NHEJ (Chen et al., 2012; Poulsen et al., 2012). RNF168 recruitment itself was found to be modulated by two other E3 ligases, TRIP12 and UBR5 (Gudjonsson et al., 2012).

Here we add another control layer to this cascade: the careful regulation of the extent of protein ubiquitylation at the damage sites by an E3/E4 ubiquitin ligase, UBE4A. Recently, Ackermann et al. (2016) reported that, in *C. elegans*, UFD-2 was involved in the DDR in the worm's gonad in a different capacity than that of UBE4A's role in the DSB response reported here. In that organism, the E3/E4 ligase plays a role in the decision between cell survival and apoptosis following induction of DNA damage. Despite the different pathways, the work of Ackermann et al. (2016) and our data indicate that meticulous shaping of ubiquitin chains by an E3/E4 ligase is essential for proper DDR throughout evolution.

Our mechanistic insight into the actual role of UBE4A-mediated ubiquitylation highlights the tight regulation of the balance between DSB repair pathways. Our data demonstrate that this fine-tuned regulatory system is abrogated in the absence of UBE4A as a result of improper accumulation and organization at DSB sites of its components. This ultimately leads, on one hand, to retarded formation of the BRCC complex that is necessary for HRR and, on the other hand, to incomplete end resection at DSB sites, another critical step in the HRR pathway. Subsequently, the resection intermediates are used by the highly error-prone alt-NHEJ pathway rather than the error-free HRR (Figure 7G). Both HRR and alt-NHEJ rely on end resection, and the extent of this critical step in DSB repair is subject to stringent regulation (Symington, 2016). Because HRR requires longer single-stranded 3′ overhangs, it is plausible that insufficiently resected overhangs will serve as alt-NHEJ substrates. Indeed, HRR deficiency because of deletions of RAD51 or RAD52 in yeast elevates alt-NHEJ (also called microhomology-mediated end-joining [MMEJ]) (Deng et al., 2014; Villarreal et al., 2012), and alt-NHEJ is elevated in human cells following BRCA1 elimination (Yun and Hiom, 2009).

The emerging picture is one of successive action of E3 ligases followed by an E3/E4 ligase, collectively carefully and meticulously shaping the ubiquitylation landscape around the break site. The exact sculpting of this landscape is essential for accurate protein dynamics and subsequent DSB repair. This process is intolerant of even the slightest perturbation, which can cause delayed or aberrant DSB repair, either of which may result in genomic rearrangements. The sophisticated regulation of the DDR and the absolute requirement of every last one of its components explain why mutations that affect any one of them can lead to grave phenotypic outcomes.

STAR★METHODS

Detailed methods are provided in the online version of this paper and include the following:

- KEY RESOURCES TABLE
- CONTACT AND REAGENT RESOURCE SHARING
- METHOD DETAILS
  - High-Throughput Screen for DDR Players in the Ubiquitin Arena
  - Cell Culture and Radiation and Chemical Treatments
  - Vector Constructs
  - RNA Interference
  - Clonogenic Survival Assay
  - Immunoblotting
  - Immunoprecipitation
  - The Comet Assay
  - Immunoprecipitation of Proteins with K63-Linked Ubiquitin Chains
  - Immunostaining and Fluorescence Measurements
  - Laser Microirradiation and Imaging of Cells Expressing Ectopic, GFP-Tagged Proteins
  - Imaging and Quantitation of Ubiquitin Chains at Sites of Laser-Induced DNA Damage
  - Ubiquitin E4 Ligase Assay
  - DSB Repair Assays
  - Single Molecule Analysis of Resection Tracks (SMART)
  - Super-Resolution Imaging
- QUANTIFICATION AND STATISTICAL ANALYSIS
  - Analysis of Super-Resolution Images

calculated as the percentage of GFP-positive cells in response to I-SceI expression upon downregulation of the indicated genes, normalized against the control. The average and SD of at least three independent experiments is shown.

(F) End resection measured using the single-molecule analysis of resection tracks (SMART) assay (Cruz-García et al., 2014). Median resection length was measured 1 hr after exposing cells transfected with the indicated siRNAs to 10 Gy of IR. The average and SD of four independent experiments is shown. For each replica, at least 300 individual single-stranded DNA (ssDNA) fibers were measured. *$p < 0.05$, **$p < 0.005$.

(G) A model scheme showing the role of UBE4A-mediated modulation of protein ubiquitylation in pathway choice during DSB repair.

SUPPLEMENTAL INFORMATION

Supplemental Information includes six figures and three tables and can be found with this article online at https://doi.org/10.1016/j.molcel.2018.02.002.

ACKNOWLEDGMENTS

We thank Kay Hofmann for valuable help with designing the siRNA libraries for the high-throughput screen, Thanos Halazonetis for the anti-53BP1 antibody, Ron Hay for the anti-RNF4 antibody, Daniel Durocher for the FLAG-53BP1 construct, Niels Mailand for the K63-UIM construct and technical advice, Aaron Ciechanover and Rachel Klevit for useful advice, Björn Schumacher, Thorsten Hoppe, and Xingzhi Xu for stimulating discussions and exchange of information, and Ron Jachimowicz for critical reading of the manuscript. Work in the Y.S. laboratory is funded by research grants from the Dr. Miriam and Sheldon G. Adelson Medical Research Foundation, the A-T Children's Project, the Israel Science Foundation Joint ISF-NSFC Research Program (jointly funded by the Israel Science Foundation and the National Natural Science Foundation of China - Grant No. 998/14), and the Israel Cancer Research Fund (Professorship). T.M. and T.C.V. were supported by funding from the Intramural Research Program of the National Institutes of Health (NIH), National Cancer Institute, and the Center for Cancer Research. Work in the K.R. laboratory is supported by the Swiss National Science Foundation (31003A_141197) and the Medical Research Council, UK (MC_PC_12001/1). Work in the G.D. laboratory is supported by a discovery grant from the Natural Sciences and Engineering Research Council of Canada (RGPIN 05616). Work in the P.H. lab was supported by an R+D+I grant from the Spanish Ministry of Economy and Competitivity (SAF2013-43255-P) and an ERC starting grant (DSBRECA). Work in the E.R. laboratory is supported by NIH grants GM108119 and CA187612 and American Cancer Society grant ACS130304-RSG-16-241-01-DMC. I.S.-B. is the recipient of a Ph.D. fellowship from the University of Sevilla. D.C. was supported by a Nova Scotia graduate scholarship. K.B.B. is a Jack and Florence Berlin fellow. Y.S. is a Research Professor of the Israel Cancer Research Fund.

AUTHOR CONTRIBUTIONS

Conceptualization, Y.S., Y.Z., K.B.-B., and A.L.-B.; Methodology, Y.S., Y.Z., K.B.-B., J.-B.Y., W.L., G.D., T.M., P.H., E.R., and K.R.; Investigation, K.B.-B., Y.Z., A.L.-B., J.O., D.A.R., I.S.-B., T.C.V., D.C., Y.P., and C.L.; Writing-Original Draft, Y.S.; Writing – Review & Editing: K.B.-B., Y.Z., A.L.-B., J.O., D.A.R., I.S.-B., T.C.V., D.C., Y.P., C.L., J.-B.Y., W.L., G.D., T.M., P.H., E.R., and K.R.; Supervision, Y.S., Y.Z., J.-B.Y., W.L., G.D., T.M., P.H., E.R., and K.R.; Project Administration, Y.S.; Funding Acquisition, Y.S., J.-B.Y., W.L., G.D., T.M., P.H., E.R., and K.R.

DECLARATION OF INTERESTS

The authors declare no competing interests.

Received: March 6, 2016
Revised: December 12, 2017
Accepted: January 31, 2018
Published: March 1, 2018

REFERENCES

Ackermann, L., Schell, M., Pokrzywa, W., Kevei, É., Gartner, A., Schumacher, B., and Hoppe, T. (2016). E4 ligase-specific ubiquitination hubs coordinate DNA double-strand-break repair and apoptosis. Nat. Struct. Mol. Biol. *23*, 995–1002.

Aravind, L., and Koonin, E.V. (2000). The U box is a modified RING finger - a common domain in ubiquitination. Curr. Biol. *10*, R132–R134.

Baek, G.H., Cheng, H., Choe, V., Bao, X., Shao, J., Luo, S., and Rao, H. (2013). Cdc48: a swiss army knife of cell biology. J. Amino Acids *2013*, 183421.

Bennardo, N., Cheng, A., Huang, N., and Stark, J.M. (2008). Alternative-NHEJ is a mechanistically distinct pathway of mammalian chromosome break repair. PLoS Genet. *4*, e1000110.

Britton, S., Coates, J., and Jackson, S.P. (2013). A new method for high-resolution imaging of Ku foci to decipher mechanisms of DNA double-strand break repair. J. Cell Biol. *202*, 579–595.

Chang, H.H.Y., Pannunzio, N.R., Adachi, N., and Lieber, M.R. (2017). Non-homologous DNA end joining and alternative pathways to double-strand break repair. Nat. Rev. Mol. Cell Biol. *18*, 495–506.

Chen, J., Feng, W., Jiang, J., Deng, Y., and Huen, M.S. (2012). Ring finger protein RNF169 antagonizes the ubiquitin-dependent signaling cascade at sites of DNA damage. J. Biol. Chem. *287*, 27715–27722.

Chen, Y.H., Jones, M.J., Yin, Y., Crist, S.B., Colnaghi, L., Sims, R.J., 3rd, Rothenberg, E., Jallepalli, P.V., and Huang, T.T. (2015). ATR-mediated phosphorylation of FANCI regulates dormant origin firing in response to replication stress. Mol. Cell *58*, 323–338.

Coleman, K.A., and Greenberg, R.A. (2011). The BRCA1-RAP80 complex regulates DNA repair mechanism utilization by restricting end resection. J. Biol. Chem. *286*, 13669–13680.

Conlin, M.P., Reid, D.A., Small, G.W., Chang, H.H., Watanabe, G., Lieber, M.R., Ramsden, D.A., and Rothenberg, E. (2017). DNA ligase IV guides end-processing choice during nonhomologous end joining. Cell Rep. *20*, 2810–2819.

Cruz-García, A., López-Saavedra, A., and Huertas, P. (2014). BRCA1 accelerates CtIP-mediated DNA-end resection. Cell Rep. *9*, 451–459.

Daley, J.M., and Sung, P. (2014). 53BP1, BRCA1, and the choice between recombination and end joining at DNA double-strand breaks. Mol. Cell. Biol. *34*, 1380–1388.

Dani, A., Huang, B., Bergan, J., Dulac, C., and Zhuang, X. (2010). Superresolution imaging of chemical synapses in the brain. Neuron *68*, 843–856.

Dantuma, N.P., Lindsten, K., Glas, R., Jellne, M., and Masucci, M.G. (2000). Short-lived green fluorescent proteins for quantifying ubiquitin/proteasome-dependent proteolysis in living cells. Nat. Biotechnol. *18*, 538–543.

Dellaire, G., Kepkay, R., and Bazett-Jones, D.P. (2009). High resolution imaging of changes in the structure and spatial organization of chromatin, gamma-H2A.X and the MRN complex within etoposide-induced DNA repair foci. Cell Cycle *8*, 3750–3769.

Deng, S.K., Gibb, B., de Almeida, M.J., Greene, E.C., and Symington, L.S. (2014). RPA antagonizes microhomology-mediated repair of DNA double-strand breaks. Nat. Struct. Mol. Biol. *21*, 405–412.

Doksani, Y., Wu, J.Y., de Lange, T., and Zhuang, X. (2013). Super-resolution fluorescence imaging of telomeres reveals TRF2-dependent T-loop formation. Cell *155*, 345–356.

Du, C., Wu, H., and Leng, R.P. (2016). UBE4B targets phosphorylated p53 at serines 15 and 392 for degradation. Oncotarget *7*, 2823–2836.

Glei, M., Schneider, T., and Schlörmann, W. (2016). Comet assay: an essential tool in toxicological research. Arch. Toxicol. *90*, 2315–2336.

Goldstein, M., and Kastan, M.B. (2015). The DNA damage response: implications for tumor responses to radiation and chemotherapy. Annu. Rev. Med. *66*, 129–143.

Goodarzi, A.A., and Jeggo, P.A. (2013). The repair and signaling responses to DNA double-strand breaks. Adv. Genet. *82*, 1–45.

Gudjonsson, T., Altmeyer, M., Savic, V., Toledo, L., Dinant, C., Grøfte, M., Bartkova, J., Poulsen, M., Oka, Y., Bekker-Jensen, S., et al. (2012). TRIP12 and UBR5 suppress spreading of chromatin ubiquitylation at damaged chromosomes. Cell *150*, 697–709.

Gupta, A., Hunt, C.R., Chakraborty, S., Pandita, R.K., Yordy, J., Ramnarain, D.B., Horikoshi, N., and Pandita, T.K. (2014). Role of 53BP1 in the regulation of DNA double-strand break repair pathway choice. Radiat. Res. *181*, 1–8.

Harding, S.M., and Greenberg, R.A. (2016). Choreographing the double strand break response: Ubiquitin and SUMO control of nuclear architecture. Front. Genet. *7*, 103.

Hatakeyama, S., and Nakayama, K.I. (2003). U-box proteins as a new family of ubiquitin ligases. Biochem. Biophys. Res. Commun. *302*, 635–645.

Hatakeyama, S., Yada, M., Matsumoto, M., Ishida, N., and Nakayama, K.I. (2001). U box proteins as a new family of ubiquitin-protein ligases. J. Biol. Chem. *276*, 33111–33120.

Henriques, R., Lelek, M., Fornasiero, E.F., Valtorta, F., Zimmer, C., and Mhlanga, M.M. (2010). QuickPALM: 3D real-time photoactivation nanoscopy image processing in ImageJ. Nat. Methods *7*, 339–340.

Hoppe, T. (2005). Multiubiquitylation by E4 enzymes: 'one size' doesn't fit all. Trends Biochem. Sci. *30*, 183–187.

Huang, B., Bates, M., and Zhuang, X. (2009). Super-resolution fluorescence microscopy. Annu. Rev. Biochem. *78*, 993–1016.

Johnson, E.S., Ma, P.C., Ota, I.M., and Varshavsky, A. (1995). A proteolytic pathway that recognizes ubiquitin as a degradation signal. J. Biol. Chem. *270*, 17442–17456.

Kowalczykowski, S.C. (2015). An overview of the molecular mechanisms of recombinational DNA repair. Cold Spring Harb. Perspect. Biol. *7*, a016410.

Lee, B.L., Singh, A., Mark Glover, J.N., Hendzel, M.J., and Spyracopoulos, L. (2017). Molecular basis for K63-linked ubiquitination processes in double-strand DNA break repair: a focus on kinetics and dynamics. J. Mol. Biol. *429*, 3409–3429.

Liu, C., Liu, W., Ye, Y., and Li, W. (2017). Ufd2p synthesizes branched ubiquitin chains to promote the degradation of substrates modified with atypical chains. Nat. Commun. *8*, 14274.

Lombardi, P.M., Matunis, M.J., and Wolberger, C. (2017). RAP80, ubiquitin and SUMO in the DNA damage response. J. Mol. Med. (Berl.) *95*, 799–807.

Lukas, J., Lukas, C., and Bartek, J. (2011). More than just a focus: the chromatin response to DNA damage and its role in genome integrity maintenance. Nat. Cell Biol. *13*, 1161–1169.

Martin-Hernandez, K., Rodriguez-Vargas, J.M., Schreiber, V., and Dantzer, F. (2017). Expanding functions of ADP-ribosylation in the maintenance of genome integrity. Semin. Cell Dev. Biol. *63*, 92–101.

Matsumoto, M., Yada, M., Hatakeyama, S., Ishimoto, H., Tanimura, T., Tsuji, S., Kakizuka, A., Kitagawa, M., and Nakayama, K.I. (2004). Molecular clearance of ataxin-3 is regulated by a mammalian E4. EMBO J. *23*, 659–669.

Meerang, M., Ritz, D., Paliwal, S., Garajova, Z., Bosshard, M., Mailand, N., Janscak, P., Hübscher, U., Meyer, H., and Ramadan, K. (2011). The ubiquitin-selective segregase VCP/p97 orchestrates the response to DNA double-strand breaks. Nat. Cell Biol. *13*, 1376–1382.

Panier, S., and Durocher, D. (2013). Push back to respond better: regulatory inhibition of the DNA double-strand break response. Nat. Rev. Mol. Cell Biol. *14*, 661–672.

Park, Y., Yoon, S.K., and Yoon, J.B. (2008). TRIP12 functions as an E3 ubiquitin ligase of APP-BP1. Biochem. Biophys. Res. Commun. *374*, 294–298.

Park, Y., Yoon, S.K., and Yoon, J.B. (2009). The HECT domain of TRIP12 ubiquitinates substrates of the ubiquitin fusion degradation pathway. J. Biol. Chem. *284*, 1540–1549.

Park, J.Y., Zhang, F., and Andreassen, P.R. (2014). PALB2: the hub of a network of tumor suppressors involved in DNA damage responses. Biochim. Biophys. Acta *1846*, 263–275.

Paull, T.T. (2015). Mechanisms of ATM Activation. Annu. Rev. Biochem. *84*, 711–738.

Pellegrino, S., and Altmeyer, M. (2016). Interplay between Ubiquitin, SUMO, and Poly(ADP-Ribose) in the cellular response to genotoxic stress. Front. Genet. *7*, 63.

Periz, G., Lu, J., Zhang, T., Kankel, M.W., Jablonski, A.M., Kalb, R., McCampbell, A., and Wang, J. (2015). Regulation of protein quality control by UBE4B and LSD1 through p53-mediated transcription. PLoS Biol. *13*, e1002114.

Pierce, A.J., Hu, P., Han, M., Ellis, N., and Jasin, M. (2001). Ku DNA end-binding protein modulates homologous repair of double-strand breaks in mammalian cells. Genes Dev. *15*, 3237–3242.

Pinder, J., Salsman, J., and Dellaire, G. (2015). Nuclear domain 'knock-in' screen for the evaluation and identification of small molecule enhancers of CRISPR-based genome editing. Nucleic Acids Res. *43*, 9379–9392.

Polo, S.E., and Jackson, S.P. (2011). Dynamics of DNA damage response proteins at DNA breaks: a focus on protein modifications. Genes Dev. *25*, 409–433.

Poulsen, M., Lukas, C., Lukas, J., Bekker-Jensen, S., and Mailand, N. (2012). Human RNF169 is a negative regulator of the ubiquitin-dependent response to DNA double-strand breaks. J. Cell Biol. *197*, 189–199.

Ramadan, K. (2012). p97/VCP- and Lys48-linked polyubiquitination form a new signaling pathway in DNA damage response. Cell Cycle *11*, 1062–1069.

Reid, D.A., Keegan, S., Leo-Macias, A., Watanabe, G., Strande, N.T., Chang, H.H., Oksuz, B.A., Fenyo, D., Lieber, M.R., Ramsden, D.A., and Rothenberg, E. (2015). Organization and dynamics of the nonhomologous end-joining machinery during DNA double-strand break repair. Proc. Natl. Acad. Sci. USA *112*, E2575–E2584.

Saeki, Y., Tayama, Y., Toh-e, A., and Yokosawa, H. (2004). Definitive evidence for Ufd2-catalyzed elongation of the ubiquitin chain through Lys48 linkage. Biochem. Biophys. Res. Commun. *320*, 840–845.

Segal-Raz, H., Mass, G., Baranes-Bachar, K., Lerenthal, Y., Wang, S.Y., Chung, Y.M., Ziv-Lehrman, S., Ström, C.E., Helleday, T., Hu, M.C., et al. (2011). ATM-mediated phosphorylation of polynucleotide kinase/phosphatase is required for effective DNA double-strand break repair. EMBO Rep. *12*, 713–719.

Shibata, A., and Jeggo, P.A. (2014). DNA double-strand break repair in a cellular context. Clin. Oncol. (R. Coll. Radiol.) *26*, 243–249.

Shiloh, Y., and Ziv, Y. (2013). The ATM protein kinase: regulating the cellular response to genotoxic stress, and more. Nat. Rev. Mol. Cell Biol. *14*, 197–210.

Sims, J.J., Scavone, F., Cooper, E.M., Kane, L.A., Youle, R.J., Boeke, J.D., and Cohen, R.E. (2012). Polyubiquitin-sensor proteins reveal localization and linkage-type dependence of cellular ubiquitin signaling. Nat. Methods *9*, 303–309.

Sirbu, B.M., and Cortez, D. (2013). DNA damage response: three levels of DNA repair regulation. Cold Spring Harb. Perspect. Biol. *5*, a012724.

Spasser, L., and Brik, A. (2012). Chemistry and biology of the ubiquitin signal. Angew. Chem. Int.Engl. *51*, 6840–6862.

Starita, L.M., Pruneda, J.N., Lo, R.S., Fowler, D.M., Kim, H.J., Hiatt, J.B., Shendure, J., Brzovic, P.S., Fields, S., and Klevit, R.E. (2013). Activity-enhancing mutations in an E3 ubiquitin ligase identified by high-throughput mutagenesis. Proc. Natl. Acad. Sci. USA *110*, E1263–E1272.

Sun, Y., Jia, X., Gao, Q., Liu, X., and Hou, L. (2017). The ubiquitin ligase UBE4A inhibits prostate cancer progression by targeting interleukin-like EMT inducer (ILEI). IUBMB Life *69*, 16–21.

Symington, L.S. (2016). Mechanism and regulation of DNA end resection in eukaryotes. Crit. Rev. Biochem. Mol. Biol. *51*, 195–212.

Thorslund, T., Ripplinger, A., Hoffmann, S., Wild, T., Uckelmann, M., Villumsen, B., Narita, T., Sixma, T.K., Choudhary, C., Bekker-Jensen, S., and Mailand, N. (2015). Histone H1 couples initiation and amplification of ubiquitin signalling after DNA damage. Nature *527*, 389–393.

Torrecilla, I., Oehler, J., and Ramadan, K. (2017). The role of ubiquitin-dependent segregase p97 (VCP or Cdc48) in chromatin dynamics after DNA double strand breaks. Philos. Trans. R. Soc. Lond. B Biol. Sci. *372*, 20160282.

Typas, D., Luijsterburg, M.S., Wiegant, W.W., Diakatou, M., Helfricht, A., Thijssen, P.E., van den Broek, B., Mullenders, L.H., and van Attikum, H. (2015). The de-ubiquitylating enzymes USP26 and USP37 regulate homologous recombination by counteracting RAP80. Nucleic Acids Res. *43*, 6919–6933.

van de Linde, S., Löschberger, A., Klein, T., Heidbreder, M., Wolter, S., Heilemann, M., and Sauer, M. (2011). Direct stochastic optical reconstruction microscopy with standard fluorescent probes. Nat. Protoc. *6*, 991–1009.

Villarreal, D.D., Lee, K., Deem, A., Shim, E.Y., Malkova, A., and Lee, S.E. (2012). Microhomology directs diverse DNA break repair pathways and chromosomal translocations. PLoS Genet. *8*, e1003026.

Wani, A.H., Boettiger, A.N., Schorderet, P., Ergun, A., Münger, C., Sadreyev, R.I., Zhuang, X., Kingston, R.E., and Francis, N.J. (2016). Chromatin topology is coupled to Polycomb group protein subnuclear organization. Nat. Commun. *7*, 10291.

Williamson, A., Werner, A., and Rape, M. (2013). The Colossus of ubiquitylation: decrypting a cellular code. Mol. Cell *49*, 591–600.

Wilson, M.D., and Durocher, D. (2017). Reading chromatin signatures after DNA double-strand breaks. Philos. Trans. R. Soc. Lond. B Biol. Sci. *372*, 20160280.

Wu, H., and Leng, R.P. (2011). UBE4B, a ubiquitin chain assembly factor, is required for MDM2-mediated p53 polyubiquitination and degradation. Cell Cycle *10*, 1912–1915.

Wu, H., Pomeroy, S.L., Ferreira, M., Teider, N., Mariani, J., Nakayama, K.I., Hatakeyama, S., Tron, V.A., Saltibus, L.F., Spyracopoulos, L., and Leng, R.P. (2011). UBE4B promotes Hdm2-mediated degradation of the tumor suppressor p53. Nat. Med. *17*, 347–355.

Yokoi, M., and Hanaoka, F. (2017). Two mammalian homologs of yeast Rad23, HR23A and HR23B, as multifunctional proteins. Gene *597*, 1–9.

Young, L.M., Marzio, A., Perez-Duran, P., Reid, D.A., Meredith, D.N., Roberti, D., Star, A., Rothenberg, E., Ueberheide, B., and Pagano, M. (2015). TIMELESS Forms a complex with PARP1 distinct from its complex with TIPIN and plays a role in the DNA damage response. Cell Rep. *13*, 451–459.

Yun, M.H., and Hiom, K. (2009). CtIP-BRCA1 modulates the choice of DNA double-strand-break repair pathway throughout the cell cycle. Nature *459*, 460–463.

Ziv, Y., Bielopolski, D., Galanty, Y., Lukas, C., Taya, Y., Schultz, D.C., Lukas, J., Bekker-Jensen, S., Bartek, J., and Shiloh, Y. (2006). Chromatin relaxation in response to DNA double-strand breaks is modulated by a novel ATM- and KAP-1 dependent pathway. Nat. Cell Biol. *8*, 870–876.

STAR★METHODS

KEY RESOURCES TABLE

REAGENT or RESOURCE	SOURCE	IDENTIFIER
Antibodies		
ATM	Sigma-Aldrich	A1106; RRID:AB_796190
BRCA1	Millipore	07-434; RRID: AB_2275035
BRCA2	Novus Biologicals	234403
γH2AX	Bethyl Laboratories	A300-081A; RRID: AB_203288
γH2AX	Millipore	05-636; RRID: AB_309864
HSC70	Santa Cruz	sc-7298; RRID: AB_627761
MDC1	Sigma-Aldrich	M-2444; RRID: AB_532268
RAP80	Novus Biologicals	NBP1-87156; RRID: AB_10999813
RNF4	Gift from R. Hay	N/A
RNF8	Millipore	09-813; RRID: AB_10806761
RNF168	Millipore	ABE367
RAD51	Santa Cruz	sc-8349; RRID: AB_2253533
Tubulin	Sigma-Aldrich	T5168; RRID: AB_477579
VCP	Abcam	ab11433; RRID: AB_298039
K48-Ub	Genentec	Apu2.07
K48-Ub	Millipore	Apu2 05-1307
K63-Ub	Genentec	Apu3.A8
K63-Ub	Millipore	Apu3 05-1308
53BP1	Gift from T. Halazonetis	N/A
Ubiquitin	Millipore	05-944; RRID: AB_441944
FLAG (M2 beads)	Sigma-Aldrich	F3165; RRID: AB_259529
UBE4A (for IF)	Bethyl Laboratories	A304-294A; RRID: AB_2620490
UBE4A	Abcam	ab128861; RRID: AB_11155948
UBE4B	Abcam	ab126759; RRID: AB_11144331
RAD23A	Abcam	ab108592
RAD23B	Abcam	ab88503; RRID: AB_10563326
Cyclin A2	Abcam	ab16726; RRID: AB_302478
Mouse monoclonal anti-BrdU	Amersham	RPN202
Goat Alexa 594 anti-mouse	Invitrogen	A11032; RRID: AB_141672
RAD51	GeneTex	14B4
BPXA1 - Alexa Fluor 647 Mouse Monoclonal	Santa Cruz	sc-6954; RRID: AB_626761
Tubulin (mouse monoclonal)	Sigma-Aldrich	T8328; RRID: AB_1844090
Goat polyclonal anti-rabbit IgG peroxidase	Sigma-Aldrich	5420
Sheep polyclonal anti-rabbit IgG peroxidase	Sigma-Aldrich	A5906; RRID: AB_258264
Bacterial and Virus Strains		
E. coli: BL21-DE3 competent cells	NEB	C25271
E. coli DH5α	Thermo Fisher Scientific	18265017
Chemicals, Peptides, and Recombinant Proteins		
Neocarzinostatin	Sigma-Aldrich	N9162
DNA-PK inhibitor, NU7441	Tocris Bioscience	3712
Glucose oxidase	Sigma-Aldrich	G7141
Catalase	Sigma-Aldrich	C30
Igepal CA-630	Sigma-Aldrich	I8896

(*Continued on next page*)

Continued

REAGENT or RESOURCE	SOURCE	IDENTIFIER
Paraformaldehyde (16%)	Electron Microscopy Services	I5710
Vectashield anti-fade	Vector Laboratories	H-1000
Critical Commercial Assays		
Protease inhibitor cocktail	Sigma-Aldrich	P8340
Clarity Western ECL Substrate	Bio-Rad	1705060
Experimental Models: Cell Lines		
U2-OS	ATCC	HTB-96
HeLa	ATCC	CCL-2
A549	ATCC	CCL-185
CAL51	DSMZ	ACC-302
U2OS-SA-GFP	Huertas Lab	N/A
U2OS-EJ5-GFP	Huertas Lab	N/A
U2OS-EJ2-GFP	Huertas Lab	N/A
Oligonucleotides		
siRNA targeting sequence 53BP1: GAAGGACGGAGUACUAAUA	Shiloh Lab	N/A
siRNA targeting sequence ATM: GACUUUGGCUGUCAACUUUCG	Shiloh Lab	N/A
siRNA targeting sequence BRCA1: CAGCAGTTTATTACTCACTAA	Shiloh Lab	N/A
siRNA targeting sequence CTRL: CGUACGCGGAAUACUUCGA	Shiloh Lab	N/A
siRNA targeting sequence CTRL	QIAGEN	SI03650325
siRNA targeting sequence MRE11: GCTGGATTTGTAAATCACTTT	Shiloh Lab	N/A
siRNA targeting sequence RAD23A	Thermo Scientific	L-005231-00
siRNA targeting sequence RAD23B	Thermo Scientific	L-011759-00
siRNA targeting sequence RAD51: GAGCUUGACAAACUACUUC	Shiloh Lab	N/A
siRNA targeting sequence RAP80: CCAGUUGGAGGUUUAUCAA	Shiloh Lab	N/A
siRNA targeting sequence RNF168: GGCGAAGAGCGATGGAAGA	Shiloh Lab	N/A
siRNA targeting sequence RNF4: GAAUGGACGUCUCAUCGUU	Shiloh Lab	N/A
siRNA targeting sequence RNF8: UGGACAAUUAUGGACAACA, CCAAGAACAAAGAAUUAG	Shiloh Lab	N/A
siRNA targeting sequence UBE4A #1	Thermo Scientific	J-007200-05
siRNA targeting sequence UBE4A #2	Thermo Scientific	J-007200-06
siRNA targeting sequence UBE4A #4	Thermo Scientific	J-007200-08
siRNA targeting sequence UBE4A pool	Thermo Scientific	L-007200-00
siRNA targeting sequence UBE4B	SIGMA	SASI_Hs02_00324426
siRNA targeting sequence VCP: AACAGCCAUUCUCAAACAGAA	Shiloh Lab	N/A
siLuciferase	Ramadan Lab	N/A
CGUACGCGGAAUACUUCGAtt	Ramadan Lab	N/A
Sip97 (VCP_7)	Ramadan Lab	N/A
AACAGCCAUUCUCAAACAGAAtt	Ramadan Lab	N/A
Recombinant DNA		
UBE4A cDNA cloned in pCR-BluntII-TOPO	imaGenes	IRCMp5012C066D; BC112367
siRNA-resistant GFP-UBE4A	Shiloh Lab	N/A
GFP-UBE4AΔU-box	Shiloh Lab	N/A
FLAG-53BP1	Gift from D. Durocher	N/A
GFP-K63-UIM	Gift from N. Mailand	N/A
pX330-LMNA gRNA1	Dellaire Lab	N/A
pCR2.1-Clover LMNA Donor	Dellaire Lab	N/A
piRFP670-N1	Addgene	45457

(*Continued on next page*)

Continued

REAGENT or RESOURCE	SOURCE	IDENTIFIER
Software and Algorithms		
ImageJ software with the PZfociEZ plugin	Wayne Rasband (NIH)	https://imagej.nih.gov/ij/
Comet Score software	TriTek	N/A
WiScan Hermes	Idea Bio-Medical	N/A
WiSoft Minerva image analysis software	Idea Bio-Medical	N/A
Other		
Ni-NTA agarose	QIAGEN	30210
3× FLAG peptide	Sigma-Aldrich	F4799
Sf21 cells	Thermo Fisher Scientific	B82101
pFastBac	Thermo Fisher Scientific	10360014
TNM-FH	Sigma-Aldrich	T1032
CometAssay system	Trevigen	4250-050-K

CONTACT AND REAGENT RESOURCE SHARING

Further information and requests for resources and reagents should be directed to and will be fulfilled by the Lead Contact, Yosef Shiloh (yossih@post.tau.ac.il).

METHOD DETAILS

High-Throughput Screen for DDR Players in the Ubiquitin Arena

A genetic-functional screen was carried out using two siRNA libraries representing players in ubiquitin-mediated processes in the human genome: the Ubi123 library, which contains some 600 siRNA pools targeting the expression of E1-, E2- and E3-ubiquitin ligases; and the UPS library, which contains 991 siRNA pools directed against mRNAs of players in the ubiquitin-proteasome system, members of the ubiquitin-like family of proteins and proteins containing ubiquitin binding domains. Overall, a total of 1,591 genes were screened, encoding proteins that are involved in a broad range of cellular circuits (Table S1).

Each siRNA screen was repeated 2 or 3 times in independent experiments, each carried out in duplicates. Lyophilized siRNA oligos were received in a 96-well platform in a total amount of 0.1 nmol/sample and dissolved in siRNA buffer (Dharmacon) to a 1 μM stock solution, using a JANUS automated liquid handler (Perkin-Elmer). The library was then rearrayed in 384-well daughter plates to be kept at −80°C. The MATLAB data management program was used to assign well positions to siRNAs.

siRNA was transfected using a reverse liquid transfection protocol. A layer of siRNA oligos complexed with lipids (100 nM/well) was placed in a 384-well platform using a Janus automated liquid handler. 2.5μl of OPTIMEM medium was first added to each well, followed by 2.5μl of a 1μM siRNA stock, and finally 5μL of Dharmafect-1 transfection reagent/OptiMEM mix (0.05μl Dharmafect-1 per well). Plates were incubated for 20 min at room temperature. F-89 hTERT cells were seeded at a density of 3,200 cells/well in a 15 μl volume of DMEM supplemented with 15% FCS, using a MultidropCombi automated dispenser (ThermoFisher Scientific). The cultures were incubated at 37°C for 72 hr. NCS, ATM inhibitor or DNA-PK inhibitor were added to the cells using a MultidropCombi automated dispenser (ThermoFisher Scientific). NCS was diluted in DMEM and 20μl were added per well to a final concentration of 100ng/ml or 200ng/ml. The ATM inhibitor KU-55933 and the DNA-PK inhibitor NU-7441 were diluted in DMEM supplemented with 15% FCS and used at a final concentration of 10μM. Fixation, washing and staining were performed with an EL406 Microplate automated 384-well plate washer dispenser (BioTek). Cells were fixed by adding 20 μl per well of 12% paraformaldehyde in PBS into the culture medium (resulting in a final concentration of 4% paraformaldehyde), and the cultures were left for 15 min at room temperature. Cells were then washed once with PBS, 20 μl of 0.5% Triton X-100 were added, and the plates were left for 10 min at room temperature and subsequently washed twice with PBS. Primary antibodies were added for 2 hr at room temperature, the plates were washed 3 times with PBS, and secondary antibodies were added. After 40 min at room temperature, DRAQ5 (diluted 1:2000) was added for an additional 20 min, and the plates were washed 4 times with PBS.

Automated imaging was carried out using the Opera system (Perkin Elmer). For counting 53BP1 foci, we imaged 24 confocal fields per well at 40X magnification; for the KAP-1 phosphorylation readout, we imaged 12 confocal fields per well at 20X magnification. Images were captured in an automated fashion in 2 channels using a 488 nm excitation laser (GFP) and a 640 nm excitation laser (DRAQ5). Typically, 300-600 cells were imaged per well. Images were analyzed using the Acapella software package (Perkin-Elmer). Nuclei were identified and masked, areas around the nuclei were determined (by the DRAQ5 channel) and laid over the 488 channel, and the signal within the nuclei was measured. Reads were analyzed using the cellHTS2 software package, based on R programming language. Quality control parameters were calculated, such as outliers between replicate measurements, plate effects, and other artifacts. siRNAs leading to cytotoxic effect, reflected in the number of cells at the end of the experiment, and hits due to plate

edge effect were excluded from the hit list. Quantitative data from all experimental repeats were then normalized by dividing each measurement by the median value across wells, annotated as samples, and assigning Z-scores.

The siGenome siRNA pools of Dharmacon were used in the initial screen, in which human Tert-immortalized fibroblasts seeded in 384-microwell plates were reverse-transfected with siRNAs and 72 hr later the cells were treated with 100 ng/ml or 200 ng/ml of the radiomimetic drug, neocarzinostatin (NCS). Control wells were incubated with ATM or DNA-PK inhibitor for 1 hr prior to NCS treatment. Cells were fixed 30 min or 24 hr after NCS treatment and stained with antibodies. Two immunofluorescence-based DDR readouts were recorded: phosphorylation of the KAP-1 protein, an ATM target, detected using specific phospho-antibody (Ziv et al., 2006), 30 min and 24 hr after applying NCS to the cultures; and the number of 53BP1 nuclear foci 24 hr after NCS treatment. Three such screens were carried out in duplicates, and Z-scores were obtained for each siRNA pool for each of the readouts.

The results demonstrated good correlation between replicates, suggesting high reproducibility (Spearman rank correlation coefficient = 0.7). The overall Z' factor calculated for the screen was 0.78, indicating that the assays used had a robust signal-to-noise ratio. Analysis across all siRNAs showed a diverse range of KAP-1 phosphorylation intensities following downregulation of various genes. Hits were defined as siRNAs that led to increased response deviating from the mean by more than 2.5 standard deviations, or decreased the response by more than 2 standard deviations.

A total of 102 genes were regarded as hits in this primary screen (Table S2), among them known DDR players such as ATM, ATR, TOPBP1 and the E3 ligases, RNF8 and RNF168. We selected 43 of them for a secondary screen, based on their functional information obtained from the literature or using bioinformatic analysis. The secondary screen was based on the same assays used in the primary one, and ON-TARGET plus siRNA pools (Dharmacon) were used. The secondary screen was repeated twice, in triplicates. 21 siRNA pools (not including the positive control, RNF8) showed similar effects as in the primary screen (Table S3).

Cell Culture and Radiation and Chemical Treatments

U2-OS, HeLa, A549 and CAL51 cells were grown in DMEM with 10% fetal bovine serum at 37°C in 5% CO_2 atmosphere. Cells were irradiated using an X-ray instrument (model 160HF, Philips, Germany). NCS and the DNA-PK inhibitor, NU7441, were diluted in phosphate-buffered saline prior to addition to the culture medium.

Vector Constructs

Full-length UBE4A cDNA cloned in pCR-BluntII-TOPO was obtained from imaGenes (IRCMp5012C066D; BC112367), PCR amplified, and cloned into pEGFP-C1 (Clontech, Mountain View, CA) using HindIII and SmaI restriction sites. siRNA-resistant GFP-UBE4A cDNA was generated by introducing into it 3 silent point mutations (T1887C, G1893T, T1896G), making it resistant to siRNA #2 against UBE4A. The GFP-UBE4AΔU-box construct was obtained by deleting the region spanned by aa 980-1049.

RNA Interference

siRNA oligonucleotides were transfected into cells using Dharmafect-1 (Dharmacon) according to the manufacturer's instructions.

Clonogenic Survival Assay

CAL51 cells were plated in triplicate at densities of 100–3000 cells per 60 mm plate and incubated for 24 hr before exposure to various doses of NCS. After 2 weeks in culture, cell colonies were fixed and stained with 0.2% crystal violet in 50% ethanol. Colonies were counted under a dissection microscope.

Immunoblotting

Cell lysates were obtained by lysing washed cells with NP-40 buffer (0.5% Igepal CA-630, 150 mM NaCl, 50 mM Tris-HCl, pH 8) containing protease inhibitor cocktail, and kept on ice for 10 min. Cell lysates were clarified by centrifugation and the protein concentration was quantified using the Bradford assay. Lysates were separated using SDS-PAGE and transferred onto nitrocellulose (0.2 μM). Membranes were blocked in 5% skim milk-TBST, reacted with primary antibodies, washed four times, 5 min each time with 0.1% Tween-20 (pH 7.6), and then incubated with peroxidase-conjugated secondary antibodies. Chemiluminescence was performed using Clarity Western ECL Substrate.

Immunoprecipitation

U2-OS cells were co-transfected with GFP- and FLAG-tagged expression vectors. 48 hr later, the cells were lysed in high-salt lysis buffer (50 mM Tris, pH 7.5, 300 mM NaCl, 1 mM EDTA, 1 mM DTT, 1% Triton, 20 mM N-ethylmethylamine, 10 mM iodoacetamide) in the presence of protease and phosphatase inhibitors at 4°C. After 30 min 1 mM $CaCl_2$ and 10 units of micrococcal nuclease were added and the lysates were left at room temperature for 1 hr. Soluble high salt extracts were dialyzed in IP buffer (50 mM Tris, pH 7.6, 150 mM NaCl, 1 mM EDTA, 1 mM DTT, 20 mM N-ethylmethylamine, 10 mM iodoacetamide, and protease and phosphatase inhibitors for 2 hr at 4°C. 1 mg of cell extract was incubated with 20 μl of packed anti-FLAG (M2) magnetic beads (Sigma-Aldrich) for 3 hr at 4°C. Beads were then washed five times with IP buffer and eluted in SDS-PAGE sample buffer.

The Comet Assay

Cells were treated with DNA damaging agents, harvested, and the comet procedure was performed using the CometAssay experimental system (Trevigen) according to the manufacturer's instructions. Briefly, the cells were mixed with low-melting agarose and the cell suspension was overlaid on microscope slides. Cell lysis was carried out within the agarose, after which the DNA trapped in the agarose was electrophoresed at 1 V/cm for 30 min. After staining the slides with SYBG Green dye for 10 min, images of 100 randomly selected cells per sample were captured with a Nikon eclipse 55i fluorescent microscope, and digital fluorescent images were obtained with the NIS-elements AR software. The relative length and intensity of DNA tails relative to heads is proportional to the amount of DNA damage in individual nuclei. These parameters were measured by tail moment with TriTek Comet Score software (TriTek, Sumerduck, VA).

Immunoprecipitation of Proteins with K63-Linked Ubiquitin Chains

U2-OS cells were transfected with GFP-K63-UIM (Thorslund et al., 2015). 48 hr later cells were suspended in lysis buffer (50 mM Tris, pH 7.5, 150 mM NaCl, 1 mM EDTA, 0.5% NP-40, 20 mM N-ethylmethylamine, 10 mM iodoacetamide) in the presence of protease and phosphatase inhibitors at 4°C. After 30 min, 2 mM MgCl2 and 125 units of Benzonase nuclease were added and incubation proceeded at room temperature for another 30 min. Lysates were centrifuged at 15,000 g for 30 min at 4°C and protein concentration was measured. Equivalent amounts of proteins (~0.5-1 mg) were incubated with 10 μg of GFP-TRAP beads (Chromotek, Planegg, Germany) for 2 hr at 4°C. Beads were then washed five times with IP buffer and eluted in SDS-PAGE sample buffer.

Immunostaining and Fluorescence Measurements

Nuclear foci of 53BP1 and RAD51 were quantified using ImageJ software with the PZfociEZ plugin. RAP80 and BRCA1 foci were imaged and quantified using WiScan Hermes (Idea Bio-Medical, Rishon LeTsiyon, Israel), and analyzed using WiSoft Minerva image analysis software (Idea Bio-Medical).

In order to visualize UBE4A laser stripes, cells were washed with PBS and incubated for 3 min at room temperature with CSK buffer containing 10 mM PIPES, pH 7.0, 100 mM NaCl, 300 mM sucrose, 3 mM $MgCl_2$, and 0.7% Triron X-100. The cells were then washed in PBS and incubated for another 3 min in CSK buffer supplemented with 0.3 mg/ml RNase A. The above immunofluorescence protocol was then followed.

Laser Microirradiation and Imaging of Cells Expressing Ectopic, GFP-Tagged Proteins

U2-OS cells expressing ectopic GFP-tagged proteins were plated on glass bottom dishes (MatTek, Ashland, MA) and pre-sensitized with 10 μM BrdU for 48 hr. The dishes were transferred into a microscope top-stage incubator equipped with a control system for gas mixture and humidity (Okolab, Ottaviani, Italy). DNA damage was induced on a Leica TCS SP8 confocal microscope (Leica Microsystems, Wetzlar, Germany) using a 405 nm diode laser focused through an HC PL APO 63X, 1.4-numerical aperture oil immersion objective (8% laser power, scan speed 650 ms, 40 scans). Images were acquired with the same system.

Relocalization of endogenous proteins to sites of laser-induced DNA damage was followed by immunostaining. DNA damage was induced by two-photon-based micro-irradiation obtained from an 800 nm laser beam in an LSM 510 Meta confocal microscope (Carl Zeiss, Jena, Germany). The microscope was equipped with a Spectral-Physics Mai-Tai (Deep-See) multi-photon laser system focused through a 63 × 1.25 numerical aperture oil immersion objective. Microirradiation was carried out at 8% laser power and scan speed of 1.61 μsec, with 40 repetitions at zoom × 1. A Leica TCS SP8 confocal microscope was used for imaging.

Imaging and Quantitation of Ubiquitin Chains at Sites of Laser-Induced DNA Damage

U2-OS cells were seeded onto 10 mm cover glasses No.1 (VWR), and pre-sensitized to UV-A laser exposure by supplementing the media with 10 μM BrdU 24 hr prior to irradiation. Cover glasses were transferred to LabTek chambers for laser exposure and allowed to recover for the indicated times in the incubator. The cells were irradiated using a 355 nm laser source connected to an Olympus IX71 microscope and focused through a 40X objective. Irradiation settings were as follows: velocity 50%, focus 47.2%, power 55.1%. At various time points cover glasses were transferred to 12-well plates (Greiner) and washed once with 1X PBS. For analyzing K48-linked ubiquitin chains, cells were pre-extracted with 25 mM HEPES, pH 7.4, 50 mM NaCl, 1 mM EDTA, 3 mM $MgCl_2$, 300 mM sucrose, 0.5% Triton X-100 for 2 min on ice followed by two washes with 1X PBS. For analysis of K63-linked chains, the cells were instantly fixed with 4% formaldehyde in 1X PBS for 20 min at RT. Cells were then permeabilized using 0.5% Triton X-100 in 1X PBS for 5 min at RT and blocked with 5% BSA in 1X PBS O/N at 4°C. The next day, cells were washed once with 1X PBS. Cover glasses were transferred to a wet chamber and reacted with primary antibodies diluted in 2.5% BSA in 1X PBS. (Dilutions: 1:1000 for antibodies against K48- and K63-ubiqutin linked chains and 1:500 for the anti-γH2AX antibody. Secondary antibodies: Dylight 488 anti-human and Alexa 594 donkey anti-mouse were diluted 1:100.) Incubation with primary antibodies was for 1 hr at RT. The cover glasses were then transferred back into 12-well plates and the cells were washed three times with 1X PBS before incubation with the secondary antibodies. The cells were then incubated with 1X PBS containing DAPI (1 μg/ml) for 20 min at RT and washed with 1X PBS. Cover glasses were then dipped into ddH_2O, dried, and mounted onto microscope slides (Thermo Scientific) with FluoroMount-G hard mounting medium (Interchim). Images were taken using a Nikon 90i epifluorescent microscope equipped with a Nikon DS-Qi1Mc

digital microscope camera. Images were captured using a 60X objective and exported as tif files. Image analysis was performed using the ImageJ software. The intensity of signals corresponding to ubiquitin chains was measured in areas defined by the γH2AX signal. Background fluorescent signal was subtracted.

Ubiquitin E4 Ligase Assay

Protein Purification

His6-tagged yeast Uba1, human UbcH5a, human ubiquitin, and Ub^{G76V}-GFP were expressed in *E. coli* strain BL21(DE3). Cells were cultured to OD600 of 0.5 in LB medium. Proteins were induced with 0.5 mM IPTG at 16°C O/N. Cells were collected and lysed in ice-cold lysis buffer containing 50 mM sodium phosphate, pH 8.0, 500 mM NaCl, and 10 mM imidazole. Lysates were clarified by centrifugation at 10,000 *g* for 20 min at 4°C and then incubated with Ni^{2+}-agarose beads (QIAGEN) for 4 hr at 4°C. After washing the beads extensively with lysis buffer, recombinant proteins were eluted with buffer containing 50 mM sodium phosphate (pH 8.0), 500 mM NaCl and 200 mM imidazole. Sf21FLAG-tagged human TRIP12 and human UBE4A were subcloned into a baculovirus expression vector, pFastBac (Invitrogen), and expressed in Sf21 cells. Sf21 cells were cultured at 27°C in TNM-FH (Sigma) with 5% fetal calf serum, penicillin (100 units/ml), and streptomycin (100 μg/ml). 60 hr after infection, cells were collected and lysed in ice-cold lysis buffer containing 40 mm HEPES-NaOH, pH 7.9, 150 mm NaCl, 1 mm dithiothreitol, 0.5% (v/v) Triton X-100, 10% (v/v) glycerol, 5 μg/ml leupeptin, 5 μg/ml antipain, 5 μg/ml pepstatin A, and 5 μg/ml aprotinin. Lysates were clarified by centrifugation at 10,000 *g* for 20 min at 4°C. FLAG-tagged proteins were purified by applying the supernatant onto a FLAG-M2-agarose column (Sigma-Aldrich) equilibrated with the lysis buffer. After extensive washing of the column with the lysis buffer, the bound proteins were eluted with the lysis buffer containing 0.3 mg/ml FLAG peptide (Sigma-Aldrich).

In Vitro *Ubiquitination Assay*

The reactions were performed using 800 ng of ubiquitin, 100 ng of Uba1, 250 ng of UbcH5a, 300 ng of Ub^{G76V}-GFP, and the indicated amounts of TRIP12 and UBE4A in a final volume of 20 μL of reaction buffer containing 25 mM Tris-HCl, pH 7.5, 50 mM NaCl, 5 mM ATP, 10 mM $MgCl_2$, and 1 mM dithiothreitol. Reaction mixtures were incubated at 37°C for 1 hr, terminated by the addition of 20 μL of 2X Laemmli sample buffer, and resolved by SDS-PAGE followed by immunoblotting analysis.

DSB Repair Assays

CRISPR HDR Assay

72 hr after RNAi treatment, U2-OS cells cultured in 6-well plates were harvested, washed with 1X PBS, and gently resuspended in 100 uL of Buffer R (Thermo Fisher, proprietary) for electroporation. 250 ng piRFP670-N1 (transfection control) with a 1.75:1 ratio of pX330-LaminA (1750 ng) and pCR2.1-CloverLamin donor plasmid (1000 ng) was mixed in along with 2 uL of 100 μM siRNA. Resuspended cells were electroporated using the Neon transfection system and seeded in 60 mm plates, each containing a glass coverslip. Cells were allowed to grow for 48 hr before fixation in 4% paraformaldehyde (PFA) at RT for 20 min. All washes were performed with 1X PBS, pH7.4. Cells were permeabilized with PBS containing 0.5% (8 mM) Triton X-100 at RT for 15 min. After four washes at 5 min each, cell nuclei were stained with 5 μg/mL DAPI in 1X PBS at RT for 10 min. CRISPR-mediated homology-directed repair (HDR) was then quantified by light microscopy. Briefly, after a 10 min PBS wash at RT, coverslips were mounted onto glass slides with Vectashield Antifade with clear nail polish. Slides were imaged using a 63X 1.4 NA lens on a custom-built Marianas spinning-disk confocal microscope system (Intelligent Imaging Innovations (3i), based on a Zeiss Axio Cell Observer equipped with a Yokagawa CSU-X1 spinning-disk unit, an Evolve 512 EMCCD camera, and 4 laser lines (405, 488, 560 and 640 nm). Over 500 iRFP670-positive cells were counted in each replicate to determine the mean gene-targeting efficiency, expressed as a percentage normalized to the control. Dual Clover and iRFP670 positive cells were counted as positive for HDR and data were represented as a scatterplot where each data point represents one replicate mean. Student's t test (unpaired, two-tailed) was used to compare the means from three independent replicates for each treatment condition.

Other DSB Repair Pathways

U2-OS cells bearing a single copy integration of the reporters SA-GFP (SSA), EJ2-GFP (alt-NHEJ) or EJ5-GFP (C-NHEJ) were used to analyze different DSB repair pathways. In all cases, 60,000 cells were plated in 6-well plates in duplicate, infected 24 hr later with lentiviral particles carrying the indicated shRNA, and fresh medium added 24 hr later. The next day, each duplicate culture was infected with lentiviral particles containing I-SceI–BFP expression construct at MOI 10 using 8 μg/ml polybrene in 1.5 mL of DMEM. The medium was changed 24 hr later, and after another 24 hr the cells were washed with PBS, trypsinized, neutralized with DMEM, centrifuged for 5 min at 700 g, fixed with 4% paraformaldehyde for 20 min, and collected by centrifugation. Cell pellets were washed once with PBS before resuspension in 150 μl of PBS. Samples were analyzed using a BD FACSAria with the BD FACSDiva Software v5.0.3. Four different parameters were considered: side scatter (SSC), forward scatter (FSC), blue fluorescence (407 nm violet laser BP, filter 450/40), and green fluorescence (488 nm blue laser BP, filter 530/30). Finally, the number of green cells from at least 10,000 events positive for blue fluorescence (infected with the I-SceI–BFP construct) was scored. The duplicate average was calculated for each sample. To facilitate the comparison between experiments, this ratio was normalized against the control. At least three independent experiments were carried out for each condition and the average and standard deviation of the three are presented.

Single Molecule Analysis of Resection Tracks (SMART)

Cells were grown in the presence of 10 μM BrdU for 24 hr, irradiated with 10 Gy of IR or treated with etoposide (10 μM), and harvested after 1 hr. Cells were embedded in low-melting agarose, followed by DNA extraction. DNA fibers were stretched on silanized coverslips, and the coverslips were baked for 2 hr at 65°C and incubated directly without denaturation with an anti-BrdU mouse monoclonal antibody. After washing with PBS, coverslips were incubated with the secondary antibody, mounted with ProLong® Gold Antifade Reagent (Molecular Probes), and stored at –20°C. DNA fibers were observed with a Nikon NI-E microscope and a PLAN FLOUR40 × /0.75 PHL DLL objective. Images were recorded and processed with NIS ELEMENTS Nikon software. For each experiment, at least 300 DNA fibers were analyzed, and fiber length was measured with Adobe Photoshop CS4 Extended version 11.0 (Adobe Systems Incorporated). Experiments were repeated independently four times. Statistical analysis of individual experiments was carried out using the Mann-Whitney test. The average length of resected DNA of at least three independent experiments was compared to a control using Student's t test.

Super-Resolution Imaging

Cells were extracted with cold CSK buffer containing 0.5% Triton X-100, washed with PBS, and fixed with 4% PFA prior to blocking (blocking solution: PBS containing 2% glycine, 2% BSA, 0.2% gelatin, and 50 mM NH_4Cl). Cells were stained with primary antibody in blocking solution for 1 hr at RT, washed with blocking solution, stained with secondary antibodies, and washed again with blocking solution.

Super-resolution microscopy was performed with a custom-built objective type (Leica 100X oil, 1.47NA), total internal reflection fluorescent microscope capable of excitation with 473 nm, 532 nm, and 640 nm diode-pumped solid-state lasers. Fluorescence emission was collected onto an EM-CCD camera (Andor iXon+ 897), with spectra split into two channels using a Dual-View (Photometrics) mounted after a filter wheel connected to the emission port of the microscope. The filter wheel contained dual band-pass emission filters to resolve the three channels, with the blue channel acquired alone and the red and green channels acquired together (Chen et al., 2015). Dye blinking was induced with a buffer containing 100 mM mercaptoethylamine and an additional oxygen scavenging system (1 mg/mL glucose oxidase, 0.02 mg/mL catalase, and 0.8% glucose) (Reid et al., 2015).

QUANTIFICATION AND STATISTICAL ANALYSIS

Analysis of Super-Resolution Images

Images were then reconstructed in ImageJ using the QuickPALM plugin (Henriques et al., 2010) and then used to calculate the area overlaps (Chen et al., 2015). Particle counts were normalized to the total number of particles observed for the two species. Cluster area and cluster overlap area were calculated from super resolution images using ImageJ and MATLAB code. The numbers of experiments (n) are described in the figure legends. Comparisons between siCTRL and siUBE4A groups in each experiment were performed using a two-tailed Student's t test.

Molecular Cell, Volume *69*

Supplemental Information

The Ubiquitin E3/E4 Ligase UBE4A Adjusts Protein Ubiquitylation and Accumulation at Sites of DNA Damage, Facilitating Double-Strand Break Repair

Keren Baranes-Bachar, Adva Levy-Barda, Judith Oehler, Dylan A. Reid, Isabel Soria-Bretones, Ty C. Voss, Dudley Chung, Yoon Park, Chao Liu, Jong-Bok Yoon, Wei Li, Graham Dellaire, Tom Misteli, Pablo Huertas, Eli Rothenberg, Kristijan Ramadan, Yael Ziv, and Yosef Shiloh

Supplemental Information

Supplemental figures

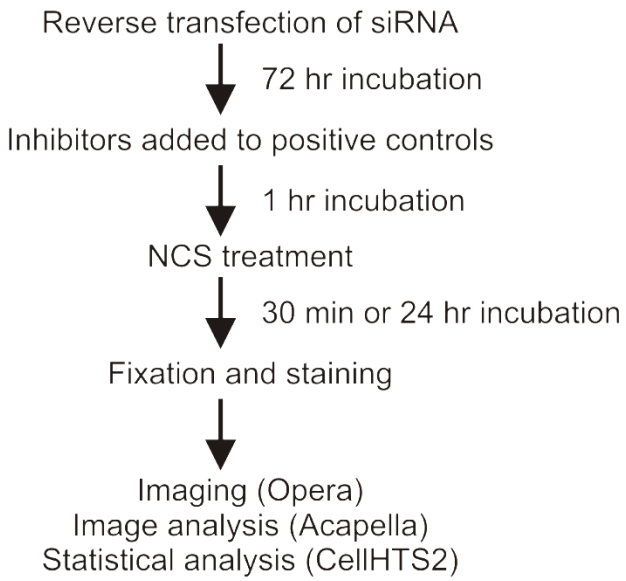

Figure S1 (Related to "High-throughput screen for DDR players in the ubiquitin arena" in the STAR Methods). Workflow of the high-throughput screen for new DDR players associated with ubiquitin-driven processes.

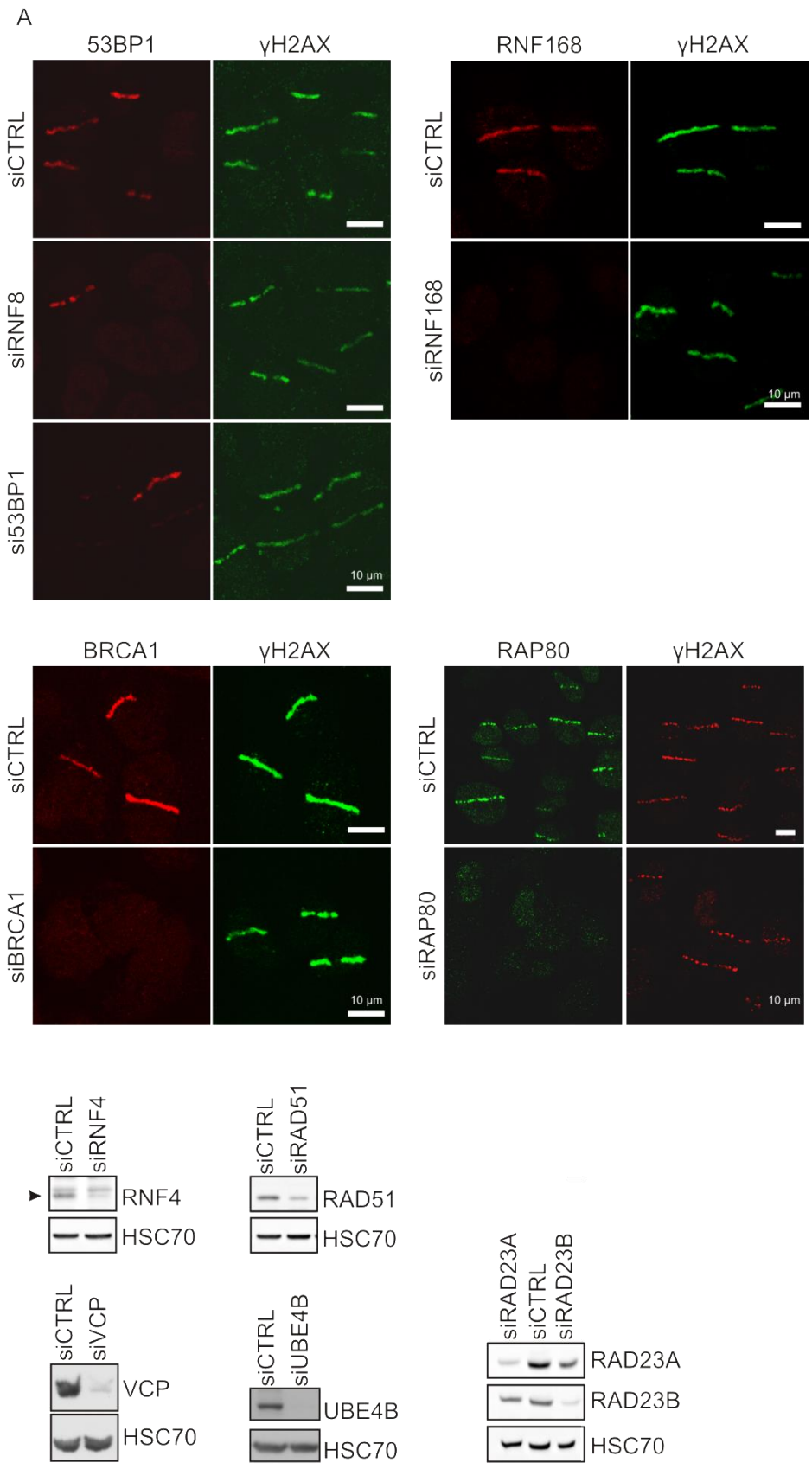
A
53BP1
γH2AX
siCTRL
siRNF8
si53BP1
10 μm
RNF168
γH2AX
siCTRL
siRNF168
10 μm
BRCA1
γH2AX
siCTRL
siBRCA1
10 μm
RAP80
γH2AX
siCTRL
siRAP80
10 μm
siCTRL
siRNF4
RNF4
HSC70
siCTRL
siRAD51
RAD51
HSC70
siCTRL
siVCP
VCP
HSC70
siCTRL
siUBE4B
UBE4B
HSC70
siRAD23A
siCTRL
siRAD23B
RAD23A
RAD23B
HSC70

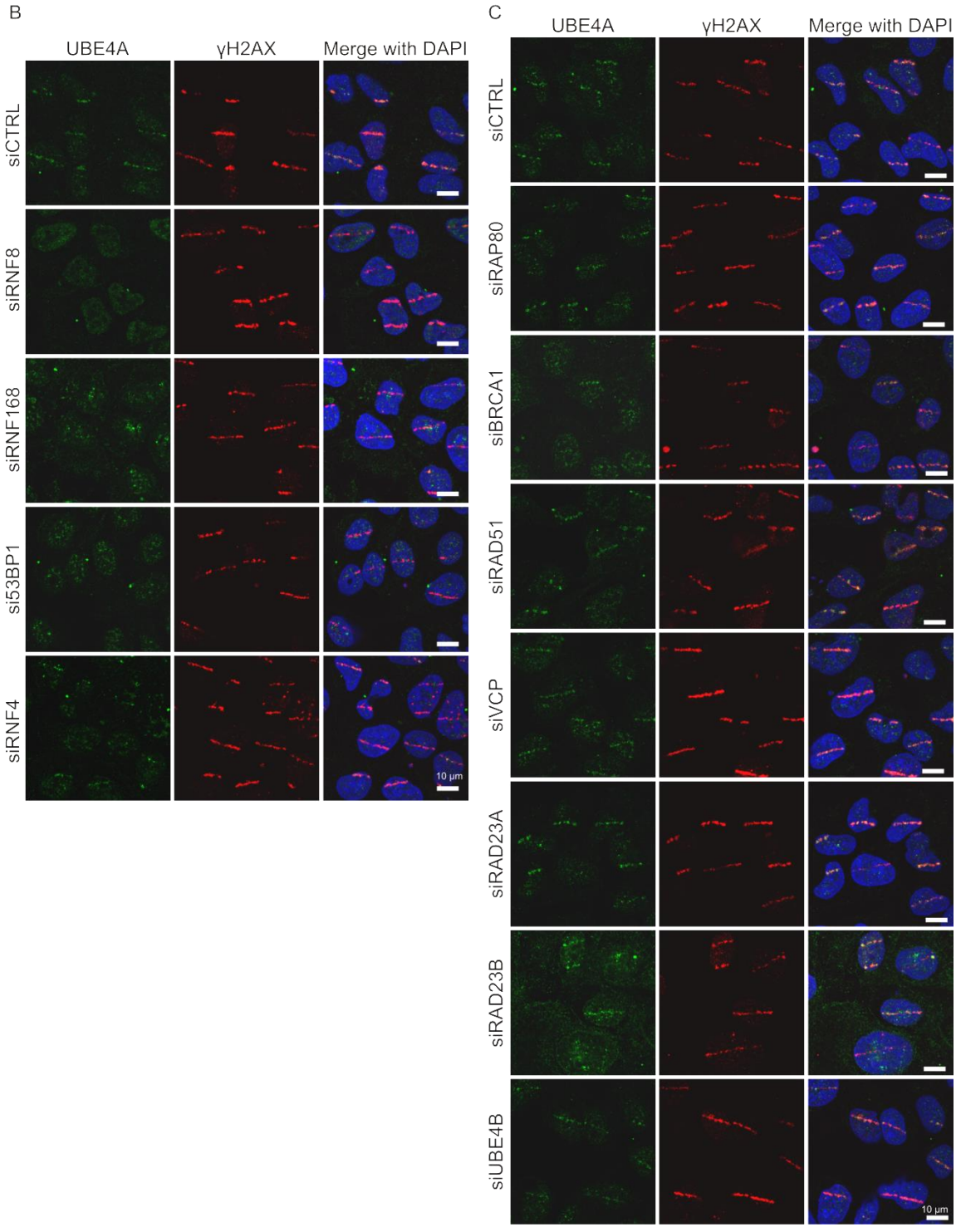
B
UBE4A
γH2AX
Merge with DAPI
siCTRL
siRNF8
siRNF168
si53BP1
siRNF4
10 μm
C
UBE4A
γH2AX
Merge with DAPI
siCTRL
siRAP80
siBRCA1
siRAD51
siVCP
siRAD23A
siRAD23B
siUBE4B
10 μm

D

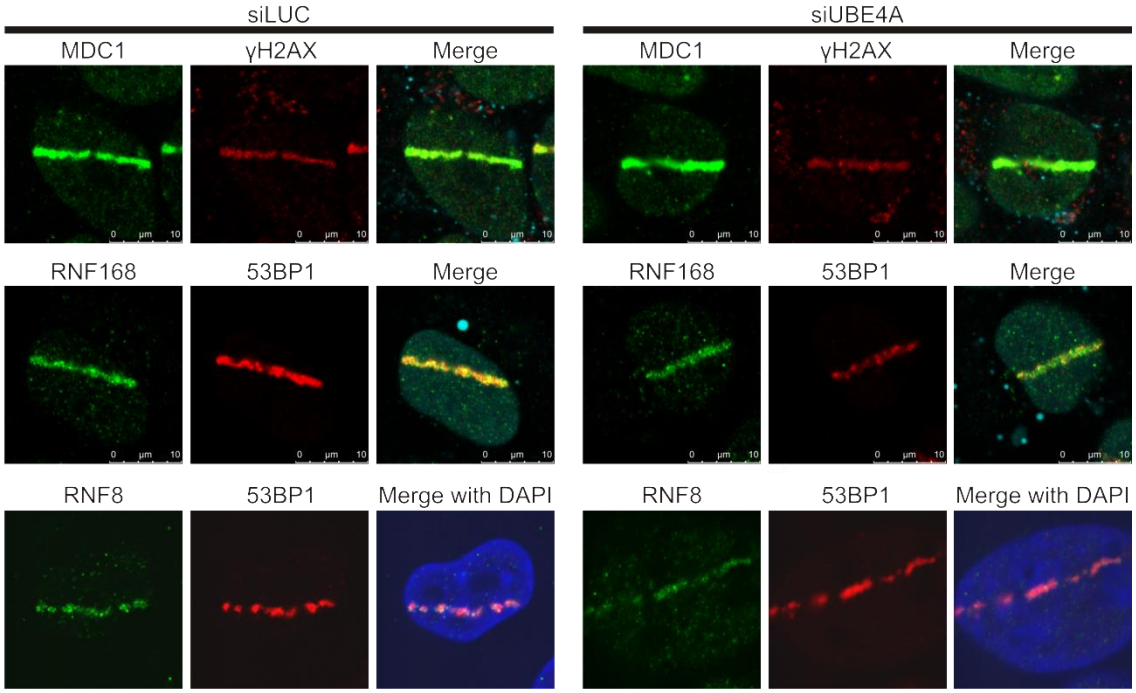
siLUC
siUBE4A
MDC1
γH2AX
Merge
MDC1
γH2AX
Merge
RNF168
53BP1
Merge
RNF168
53BP1
Merge
RNF8
53BP1
Merge with DAPI
RNF8
53BP1
Merge with DAPI

E

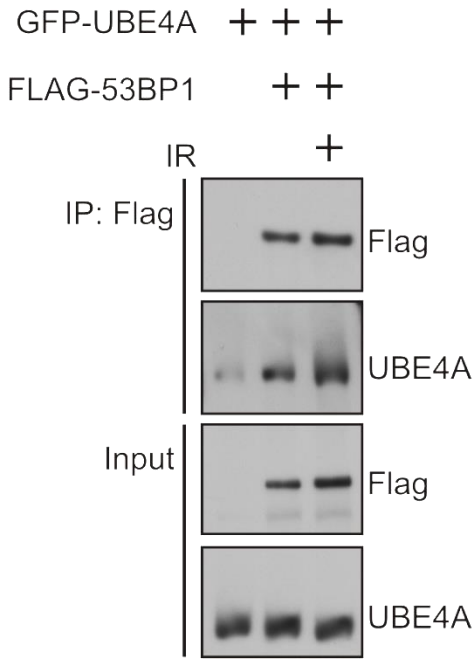
GFP-UBE4A + + +
FLAG-53BP1 + +
IR +
IP: Flag
Flag
UBE4A
Input
Flag
UBE4A

Figure S2 (Related to Figure 2). (A) Images and immunoblots demonstrating the extent of depletion of DDR players used in Fig. 2A and B. **(B, C)** Images demonstrating the effect of deletion of various DDR players on the recruitment of endogenous UBE4A to laser-induced DNA damage. **(D)** Images showing the effect of UBE4A depletion on the recruitment of other proteins to laser-induced DNA damage. Cells were transfected with the indicated siRNAs and 72-96 hr later localized DNA damage was induced by a focused laser microbeam. The cells were fixed 20 min later and stained with the indicated antibodies. Loss of 53BP1 recruitment to damage sites serves as a proxy for monitoring the depletion of RNF8. **(E)** Interaction between ectopic UBE4A and 53BP1 is enhanced following DNA damage. GFP-UBE4A and FLAG-53BP1 were co-expressed in U2-OS cells, which were irradiated with 10 Gy of IR or left untreated. Immunoprecipitation with anti-FLAG beads followed, and the immune complexes were blotted with the indicated antibodies.

A

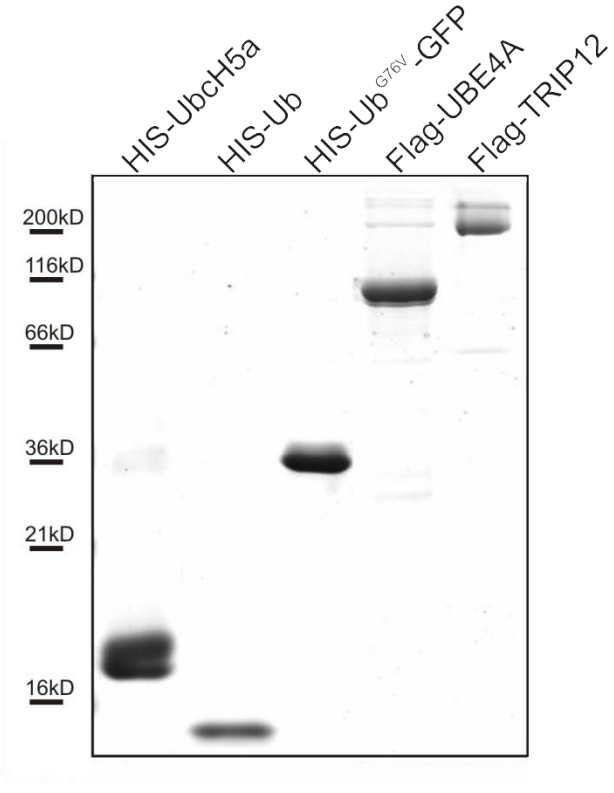

B

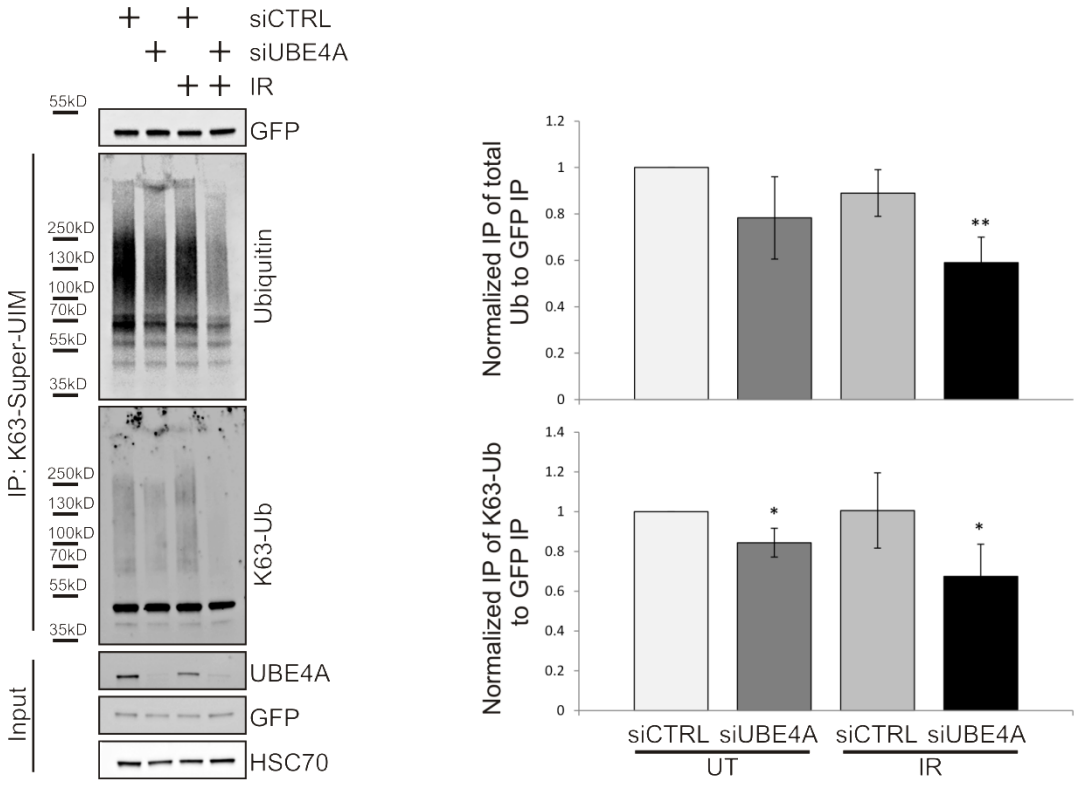

Figure S3 (Related to Figure 3). (A) Gel electrophoresis demonstrating the purification of the components used in the reactions in Figure 3. Purified recombinant proteins (400 ng) were separated on a 4–20% SDS-polyacrylamide gel and visualized using Coomassie Brilliant Blue staining. **(B)** UBE4A depletion reduces K63-mediated ubiquitylation in cells. U2-OS cell were transfected with irrelevant or UBE4A siRNA and then with a construct expressing a GFP-tagged chain of 3 ubiquitin-interacting motifs (UIMs), which bind K63-linked ubiquitin chains. The cells were treated with 10 Gy of IR or left untreated, and 2 hr after irradiation immunoprecipitation was carried out using GFP

beads. The immune complexes were blotted with antibodies against ubiquitin or K63-linked ubiquitin chains (left panel). Right panel: The signals in different lanes (left panel) were quantified using the ImageJ software and the values were normalized against the quantity of the GFP IP. Upper part - quantification of the ubiquitin signal, Lower part - quantification of K63-Ub signal.

A

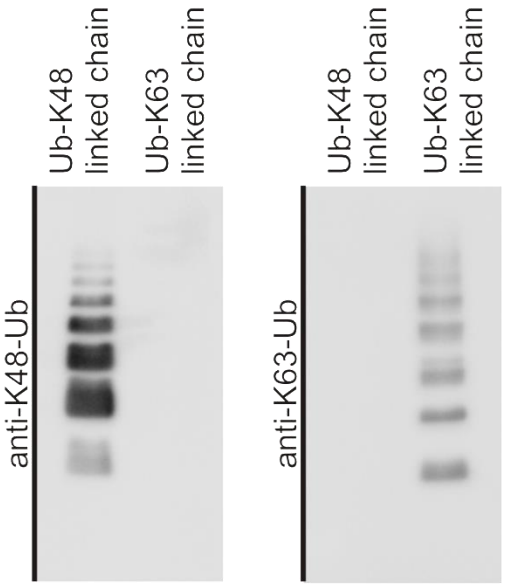

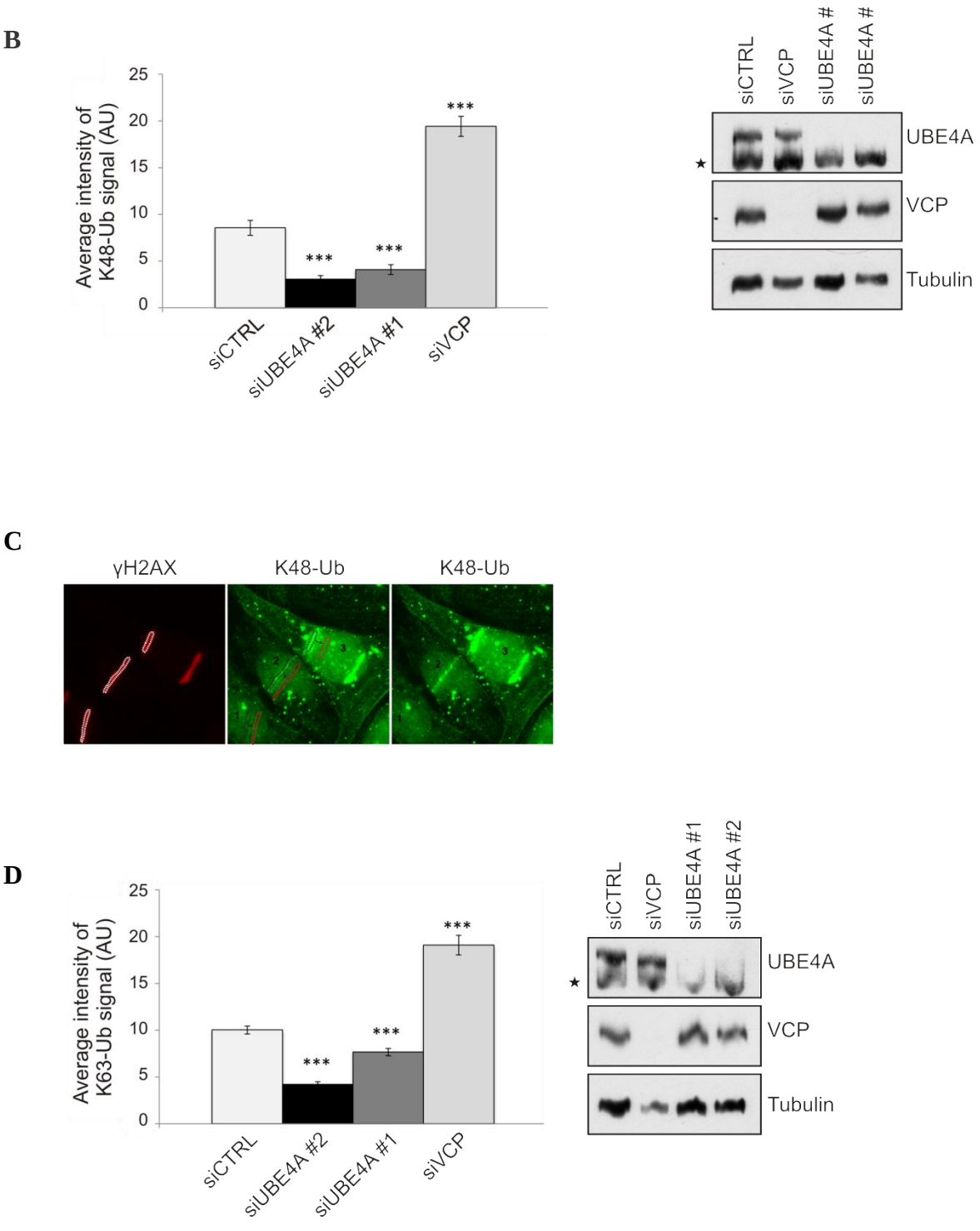

Figure S4 (Related to Figure 4). (A) Specificity of antibodies against specific ubiquitin chains. Multiubiquitin chain peptides (Ub2-7, K48 linked; Ub-K48) and (Ub2-7, K63

linked; Ub-K63) were analyzed in immunoblotting using antibodies against K48-Ub and K63-Ub. Note that, following heating and SDS-PAGE, polyubiquitin chains produce various high molecular weight multimers. **(B)** Similar analyses as in Figure 4B, demonstrating the effects of depleting UBE4A using two different siRNAs, and VCP. The immunoblots show the extent of protein depletion in these experiments. **(C)** Definition of the signal intensity of K48-linked ubiquitin chains at laser-induced damage. The areas of the γH2AX stripes (red) were defined (encircled by the while dotted lines), and the intensity of the ubiquilin chain signals (green) within the encircled areas were measured. The encircled areas were then moved within the same nuclei, away from the damage stripes (red dotted lines), and the background signals within these areas were measured and subsequently subtracted from the corresponding ubiquitin signals. The final grading of the signals was ‘undetectable’ (nucleus 1), ‘average’ (nucleus 2), and ‘strong’ (nucleus 3). **(D)** Similar analyses as in Figure 4E, demonstrating the effects of depleting UBE4A using two different siRNAs, and VCP. The immunoblots show the extent of protein depletion in these experiments. The asterisk denotes a non-specific band.

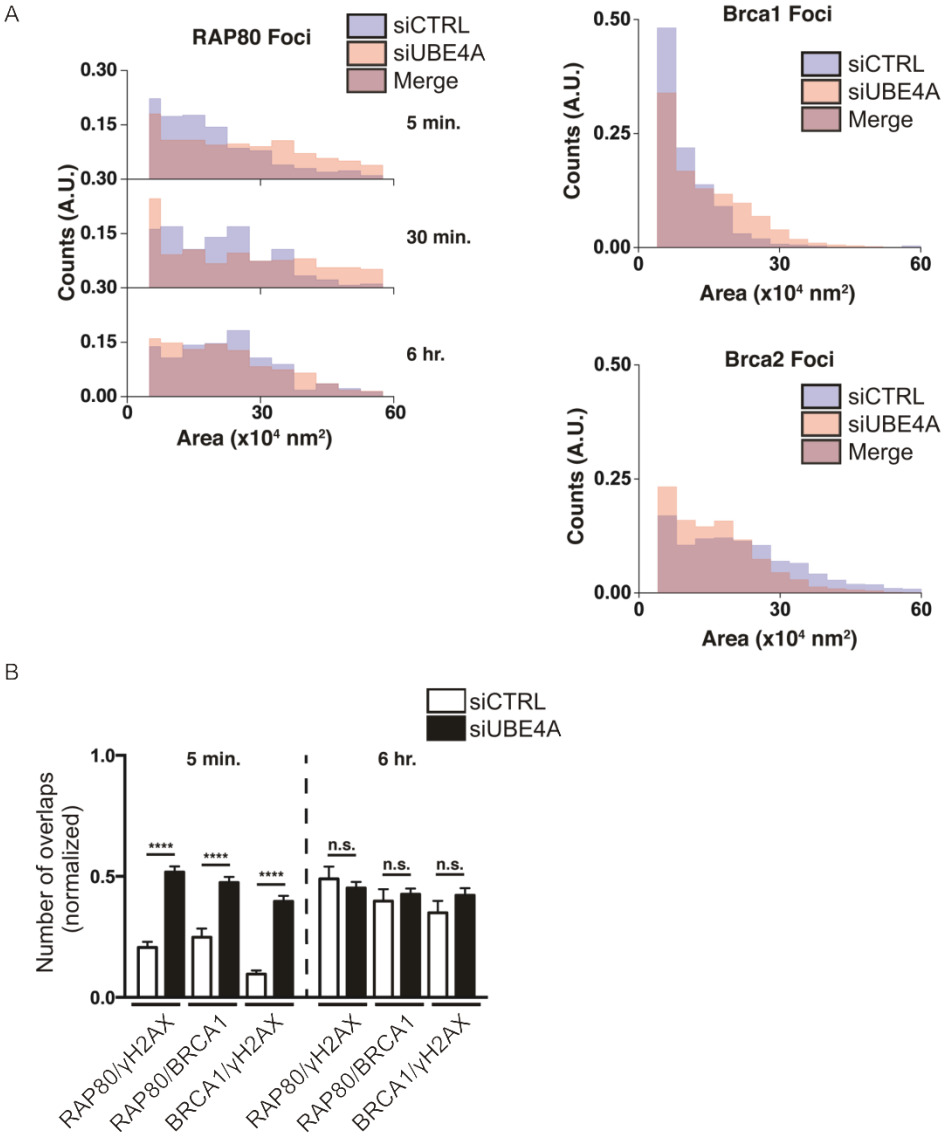

Figure S5 (Related to Figure 6). **(A)** Quantification of the size of RAP80/BRCA1/BRCA2 particles in cells transfected with control or UBE4A siRNA and treated with NCS. RAP80 measurements were made 5 min, 30 min, and 6 hr after treatment, and BRCA1 and BRCA2 measurements 30 minutes after treatment. **(B)** Number of γH2AX/RAP80, RAP80/BRCA1, and γH2AX/BRCA1 overlaps in siCTRL and siUBE4A cells, 5 min and 6 hr after NCS treatment. Quantified data represented as

mean ± SEM (2 independent experiments, n>100). Ns: not significant. **** p<0.0001 (student's t-test).

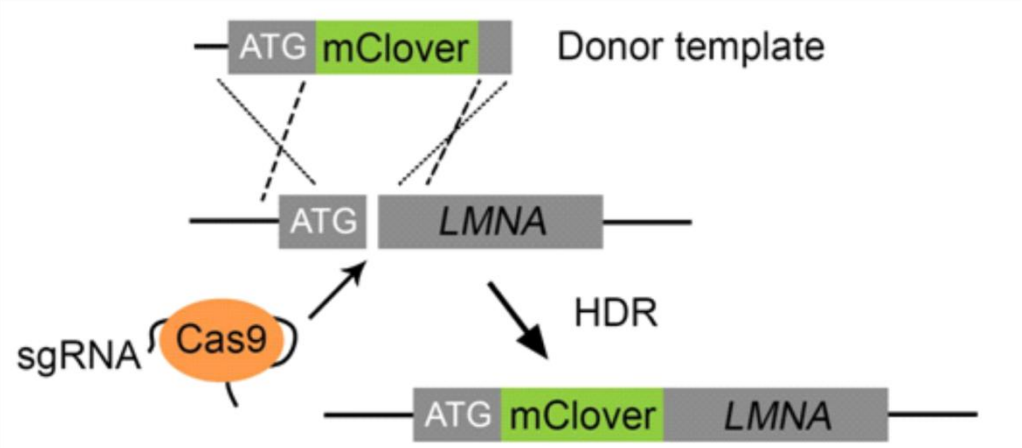

Figure S6 (Related to Figure 7B). A schematic representation of the CRISPR clover-LMNA HDR assay.